The Astrophysical Journal, 893:79 (22pp), 2020 April 10 https://doi.org/10.3847/1538-4357/ab800b

Unbiased Spectroscopic Study of the Cygnus Loop with LAMOST. I. Optical Properties of Emission Lines and the Global Spectrum

Ji Yeon Seok[1,2,6], Bon-Chul Koo[3], Gang Zhao[1,4], and John C. Raymond[5]
[1] Key Laboratory of Optical Astronomy, National Astronomical Observatories, Chinese Academy of Sciences, Beijing 100010, People's Republic of China
[2] Korea Astronomy and Space Science Institute, Daejeon, 305–348, Republic of Korea; jyseok@kasi.re.kr
[3] Seoul National University, Seoul 151–742, Republic of Korea
[4] School of Astronomy and Space Science, University of Chinese Academy of Sciences, Beijing 100049, People's Republic of China
[5] Harvard-Smithsonian Center for Astrophysics, 60 Garden Street, Cambridge, MA 02138, USA
Received 2020 January 2; revised 2020 February 26; accepted 2020 March 14; published 2020 April 17

Abstract

We present an unbiased spectroscopic study of the Galactic supernova remnant (SNR) Cygnus Loop using the Large Sky Area Multi-object Fiber Spectroscopic Telescope (LAMOST) DR5. LAMOST features both a large field of view and a large aperture, which allow us to simultaneously obtain 4000 spectra at ∼3700–9000 Å with $R \approx 1800$. The Cygnus Loop is a prototype of middle-aged SNRs, which has the advantages of being bright, large in angular size, and relatively unobscured by dust. Along the line of sight to the Cygnus Loop, 2747 LAMOST DR5 spectra are found in total, which are spatially distributed over the entire remnant. This spectral sample is free of the selection bias of most previous studies, which often focus on bright filaments or regions bright in [O III]. Visual inspection verifies that 368 spectra (13% of the total) show clear spectral features to confirm their association with the remnant. In addition, 176 spectra with line emission show ambiguity of their origin but have a possible association to the SNR. In particular, the 154 spectra dominated by the SNR emission are further analyzed by identifying emission lines and measuring their intensities. We examine distributions of physical properties such as electron density and temperature, which vary significantly inside the remnant, using theoretical models. By combining a large number of the LAMOST spectra, a global spectrum representing the Cygnus Loop is constructed, which presents characteristics of radiative shocks. Finally, we discuss the effect of the unbiased spectral sample on the global spectrum and its implication to understand a spatially unresolved SNR in a distant galaxy.

Unified Astronomy Thesaurus concepts: Supernova remnants (1667); Shocks (2086); Interstellar line emission (844)

Supporting material: figure set

1. Introduction

One of the commonalities that supernova remnants (SNRs) have shown is that their structures and physical properties are nonuniform and inhomogeneous (e.g., Williams et al. 1999; Lopez et al. 2011; Seok et al. 2013). Diversity of SNR morphologies revealed by multiwavelength band observations (e.g., Levenson et al. 1995; Rho & Petre 1998; Rho et al. 2001; Reach et al. 2002; Hines et al. 2004; Koo et al. 2016; Yamane et al. 2018) implies that their physical properties including temperature and density could strongly vary from one part to another even within a single SNR unlike the spherical symmetry that theoretical models for SNR evolution often assume (e.g., Chevalier 1974; Preite Martinez 2011). The spatial variation of the physical properties inside an individual SNR is closely related to supernova (SN) explosion mechanisms (e.g., Hwang et al. 2004; Lopez et al. 2011; Peters et al. 2013) as well as its surrounding environment (e.g., Chu 1997; Bilikova et al. 2007; Lee et al. 2012). In particular for evolved SNRs, the latter plays a significant role for characterizing the nature of each SNR.

Depending on the environment, various shock waves can be driven by SN explosions. When the ambient medium has a low density ($\leqslant 1\,\mathrm{cm}^{-3}$), such shocks are usually (nonradiative) collisionless (e.g., Raymond 1991; Draine & McKee 1993). If a collisionless shock encounters (partially) neutral pre-shock gas, the optical emission from the shock is dominated by hydrogen emission lines, and it is referred to as "Balmer-dominated" (Chevalier & Raymond 1978). When a shock has accumulated a sufficient column density (N_{H}), the energy loss via radiative cooling becomes significant. Then, the shock wave is referred to as a radiative shock. If a shock has not yet propagated enough to become fully radiative, the shock wave is incomplete (or truncated), with spectral features that differ from the emission spectrum of radiative shocks (Raymond et al. 1988). Such different types of shocks have been observed in SNRs and even inside a single SNR (e.g., see McKee & Hollenbach 1980; Raymond 1991; Draine & McKee 1993; Ghavamian et al. 2013, and references therein).

The Cygnus Loop (G74.0–8.5) is a prototypical middle-aged SNR ($1.7–2.5 \times 10^4$ yr, Miyata et al. 1994; Levenson et al. 1998; Fesen et al. 2018), which is among the brightest in optical and best-studied Galactic SNRs over the whole electromagnetic spectrum (e.g., gamma-ray: Katagiri et al. 2011, X-ray: Graham et al. 1995; Levenson et al. 1997, 1999; Uchida et al. 2009, ultraviolet: Danforth et al. 2000; Seon et al. 2006; Kim et al. 2014, optical: Miller 1974; Levenson et al. 1998; Blair et al. 2005, infrared: Braun & Strom 1986; Arendt et al. 1992; Sankrit et al. 2010, radio: Leahy et al. 1997; Leahy & Roger 1998; Leahy 2002; Uyanıker et al. 2002, 2004). It is large in angular size, covering nearly $3^\circ \times 4^\circ$ of the sky. The distance from Earth to the Cygnus Loop has been uncertain. Previous estimates range between ∼400 pc and 1 kpc, and the

[6] LAMOST Fellow.

most recent estimate is 735 ± 25 pc based on Gaia parallaxes of three stars toward the remnant (Fesen et al. 2018, and references therein). Adopting 735 pc, the physical size of the Cygnus Loop corresponds to ∼38 × 51 pc. Despite local variations in the morphology observed in different wavelengths, the overall remnant has a complete shell with the breakout to the south.

Taking advantage of its great extent, proximity, and relatively low interstellar extinction (Parker 1967; Fesen et al. 1982), detailed structures associated with diverse types of shock waves inside the Cygnus Loop have been detected and examined (e.g., Miller 1974; Raymond et al. 1980, 1988; Fesen et al. 1982; Levenson et al. 1998; Blair et al. 2005; Sankrit et al. 2014). In particular, a few selected locations including the prominent emission regions such as the Eastern and Western Veil Nebulae (NGC 6992 and NGC 6960, respectively) and the southernmost part of NGC 6992, the so called "XA" region (Hester & Cox 1986), have been extensively investigated by using imaging as well as spectroscopy (e.g., Raymond et al. 1988; Hester et al. 1994; Levenson et al. 1996; Danforth et al. 2001; Blair et al. 2005; Medina et al. 2014). Bright optical emission in these regions arises from (complete or incomplete) recombination zones behind shock waves with a velocity of $v_s \lesssim 100\,\mathrm{km\,s^{-1}}$ (e.g., Raymond et al. 1988) whereas faint Balmer-dominated filaments often found outside the bright emission regions are produced by a fast, nonradative shock with a velocity of $v_s \gtrsim 150\,\mathrm{km\,s^{-1}}$ (e.g., Blair et al. 2005).

To understand the evolution of the Loop and its large-scale influence on the ambient medium comprehensively, it is essential to examine physical (and chemical) properties of the entire remnant such as shock velocities, pre-shock densities, and abundances and take their spatial variations into account. In general, spectral and spatial information from a remnant can be obtained by performing spectral mapping or integral-field spectroscopy. Such an approach is, however, limited to small objects in angular size or one portion of a large object. For a large object like the Cygnus Loop, it is practically unfeasible to obtain spectra of the entire region in the same manner. Consequently, previous studies with optical spectroscopy often either have focused on specific regions (e.g., Raymond et al. 1988; Danforth et al. 2001; Patnaude et al. 2002) or have collected spectra from a few positions (e.g., Miller 1974; Fesen et al. 1982). On the other hand, multi-object spectroscopy with a large field of view can provide an alternative way to evaluate global properties efficiently. Recently, Medina et al. (2014) have used a multi-object echelle spectrograph, Hectochelle, mounted on the MMT 6.5 m telescope to examine collisionless shocks in the northeast limb of the Loop. High-resolution spectra covering Hα and [N II] λλ6548, 6583 (∼6460–6670 Å) were obtained from 240 locations inside the 1° region, which allowed them to constrain properties of both the pre-shock and post-shock gas around Balmer-dominated filaments.

In this paper, we present the first results of the extensive, multi-object spectroscopic observations carried out toward the entire region (4° × 4°) of the Cygnus Loop using the Large Sky Area Multi-object Fiber Spectroscopic Telescope (LAMOST) Data Release 5 (DR 5). Section 2 describes a brief overview of the LAMOST data, selection of spectra associated with the remnant, and line identification. In Section 3, we examine line ratios and their mutual correlations and derive physical properties. Then, we construct a global spectrum of the Cygnus Loop and discuss its global characteristics and implications for extragalactic SNRs in Section 4. Finally, we summarize the main results in Section 5. Detailed analysis of kinematics, spatial variation, and shock modeling will be discussed in forthcoming papers.

2. Data

2.1. LAMOST Data

We have examined the Cygnus Loop using spectra from LAMOST DR 5 released on 2017 December. LAMOST (also known as Guo Shou Jing Telescope) features both a wide field of view (∼20 deg^2) as well as a large aperture (∼4 m in diameter), and 16 spectrographs equipped with 32 4K × 4K CCDs allow us to obtain 4000 spectra simultaneously (Cui et al. 2012). Blue (3700–5900 Å) and red (5700–9000 Å) spectra are recorded separately with two CCDs. The spectral coverage is 3700–9000 Å, and a spectral resolution of $R \approx 1800$ (corresponding a velocity resolution of $\sim 167\,\mathrm{km\,s^{-1}}$) is achieved by placing slit masks of two-thirds width of the fibers (i.e., 2.″2 in diameter; Zhao et al. 2012; Luo et al. 2015). LAMOST raw data are reduced with the LAMOST 2D pipeline (Luo et al. 2015), which are similar to those of the Sloan Digital Sky Survey (Stoughton et al. 2002). The LAMOST 2D pipeline include basic pre-processing such as dark and bias subtraction, flat-fielding, and sky subtraction. The final output of the LAMOST data (combining blue and red channels) are one-dimensional relative flux-calibrated spectra. The data presented in this work are reduced using version 2.9.7 of the pipeline and can be directly downloaded from the LAMOST DR5 archive.[7] For spectra with a high signal-to-noise ratio (S/N; i.e., S/N ⩾ 30 at 4350 Å), a precision of about 10% between 4100 and 9000 Å is generally expected according to a comparison of the spectra of common objects obtained on different nights (Xiang et al. 2015). In this paper, we adopt 10% calibration error, and the final uncertainties are the quadratic sum of the calibration errors and the flux uncertainties mainly arising from the baseline fluctuation in Gaussian fitting (see Section 2.2).

The field of the Cygnus Loop is included in one of the LAMOST regular surveys, the LAMOST Experiment for Galactic Understanding and Exploration (LEGUE; Deng et al. 2012). We found 2747 LAMOST DR5 spectra in the direction of the Cygnus Loop centered at $(\alpha_{J2000}, \delta_{J2000}) = (20^h51^m, +30°40')$, which are evenly distributed over the entire SNR as shown in Figure 1. The spectra were obtained on two separate dates, the details of which are summarized in Table 1.

Because all observations are a part of the LEGUE survey primarily targeting stars, they do not particularly aim to observe the SNR itself. For this reason, many of the spectra can possibly contain stellar emission (see below). To discriminate between spectra of the Cygnus Loop and those of other objects, we first screen all spectra automatically based on the presence of emission lines (i.e., [O III] λ5007, Hα, and [S II] λλ6717, 6731), considering that most stellar spectra do not exhibit emission lines except for peculiar stellar types such as Be, Herbig Ae/Be, and Wolf–Rayet stars. By comparing the mean intensity at wavelength ranges of the emission lines and its adjacent continuum level, 778 spectra show that the mean intensity is greater than the continuum level for one emission line or more. Then, we perform visual inspection to classify

[7] http://dr5.lamost.org/

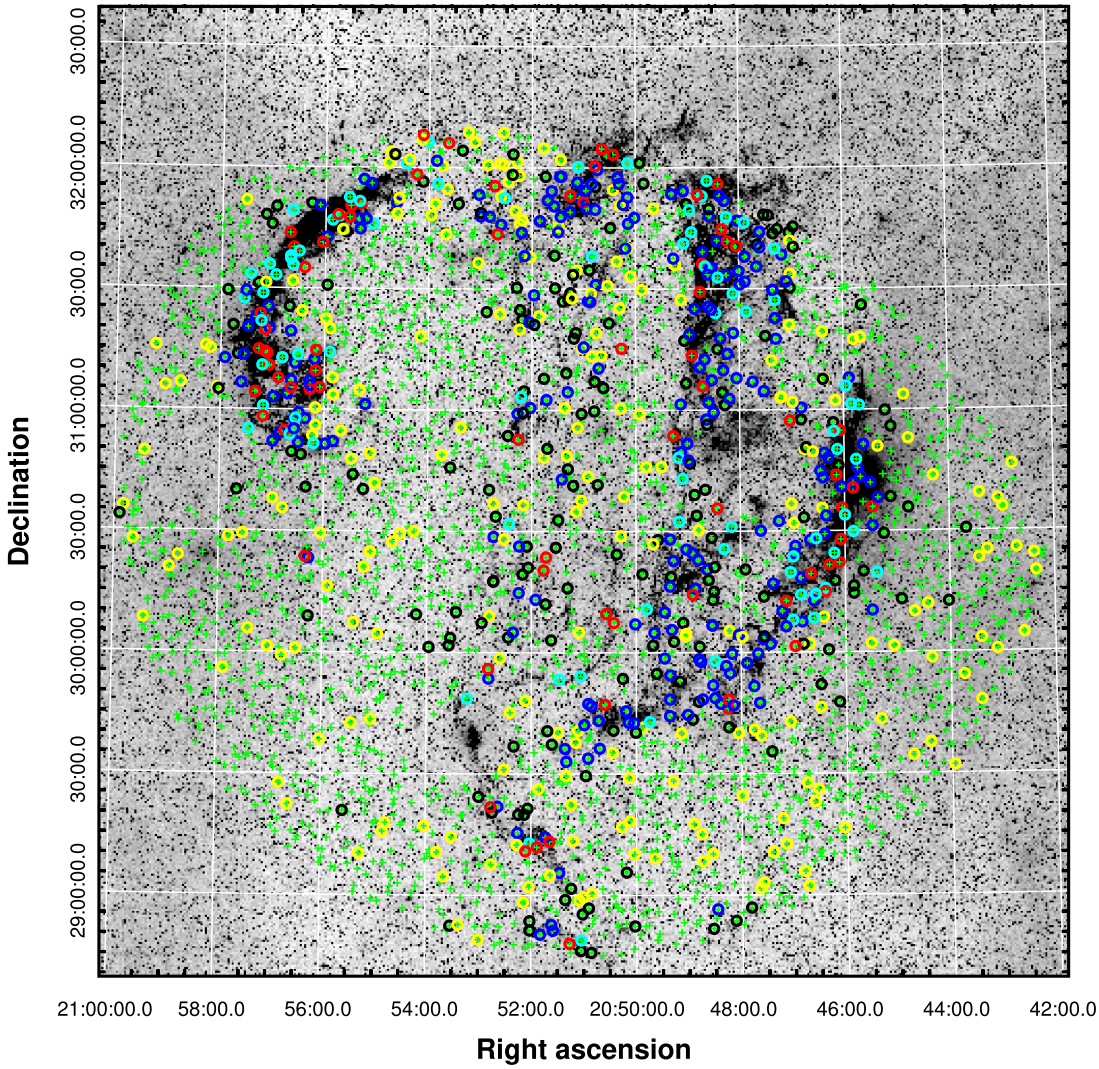

Figure 1. The Cygnus Loop reproduced from the red image of the DSS2 showing the locations of the 2747 LAMOST fibers (green crosses). Those selected for visual inspection (778 spectra, marked with circles) are classified into four groups: I. SNR-dominated spectra (red), II. SNR+stellar spectra (IIa: cyan, IIb: blue), III. Stellar spectra with tentative SNR emission or ambiguous association with the SNR (black), and IV. No association with the SNR (yellow). 75, 79, 214, 176, and 234 spectra are included in Group I, IIa, IIb, III, and IV, respectively.

them into four groups; (I) SNR-dominated spectra, (II) SNR +stellar spectra, (III) stellar spectra with tentative SNR emission or ambiguous association with the SNR, and (IV) spectra not associated with the SNR. For Group II, we divide them into two subgroups, IIa and IIb: IIa spectra exhibit as rich emission lines as Group I shows, whereas only a few lines (Hα, [N II], and [S II] lines in most cases) are clearly detected in IIb spectra. Therefore, Group I and IIa spectra are mainly used for further analysis, yet Group IIb spectra are included when only [S II] doublets are analyzed such as deriving electron densities (n_e, see Section 3.2). Finally, the numbers of spectra in Groups I, IIa, IIb, III, and IV are 75, 79, 214, 176, and 234, respectively, which are marked with different colors in Figure 1. Details of the spectrum classification are summarized in Table 2.

Group I contains 75 spectra dominated by SNR emission; Strong emission lines such as Hα, [S II], [N II], and [O III] appear clearly, and stellar features such as absorption or a continuum, if present, are negligible when SNR emission lines are extracted. Their associations with the Cygnus Loop are also confirmed by their spatial correspondences to the optical emission from the SNR seen in Figure 1. Two exemplary spectra in Group I (obs. ID 470512087 and 470512137) are presented in Figure 2. The spectrum of obs. ID 470512087 is dominated by the strong [O III] $\lambda\lambda$4959, 5007 lines whereas that of obs. ID 470512137 features the Balmer-series lines (i.e., Hα, Hβ, Hγ, etc.). All Group I spectra at the entire wavelengths (3500–8900 Å) are shown in Figure A1.

Those showing both SNR emission and stellar features are classified into Group II. This can occur when diffuse emission from the Cygnus Loop and a background or foreground star are included within a single fiber. More than one-third of the first-screened spectra (IIa + IIb: 293) belong to this category, which is a natural consequence considering the fact that the LAMOST survey primarily intends to target stellar objects in this field. Group II spectra show clear emission lines from the Cygnus

Table 1
Observation Summary

Obs. Date[a] (yyyy mm dd)	Plan ID	Seeing[b] (arcsec)	Exposure Time (s)	Number of Spectra (count)
2016 Sep 30	HD205307N293856B01	3.″2	4500	1543
2016 Nov 2	HD205307N293856V01	2.″6	1800	1204

Notes.
[a] The observation median UTC.
[b] FWHM of point-spread function measured during exposure representing the weather condition at a given date.

Table 2
Spectrum Classification for 778 Spectra After the First Screening

Group	Number	Note	Symbol Color[a]
I	75	SNR-dominated	Red
IIa	79	(strong) SNR + stellar	Cyan
IIb	214	(weak) SNR + (strong) stellar	Blue
III	176	Ambiguous, possibly Balmer-dominated	Black
IV	234	Stellar-dominated	Yellow

Notes. Groups I and IIa are mostly used for analysis in Section 3, and Group IIb is only used to estimate n_e (see Section 3.2).
[a] Symbol colors in Figure 1.

Loop as well as nonnegligible stellar features such as a series of hydrogen absorption features, Na I and Ca II absorption, and a blue (or red) stellar continuum. In Figure 2, two IIa spectra are shown: obs. ID 470514090 and 475216086. The former spectrum shows the emission lines from the SNR on top of an F-type stellar spectrum featured by strong H and K of Ca II whereas the latter shows the SNR emission as well as an M-type stellar spectrum characterized by a set of TiO bands. For this group, careful line identification is required, especially for those lines affected by strong absorption (see Section 2.2). The locations of Group II spectra (IIa and IIb marked by cyan and blue circles, respectively, in Figure 1) are spatially in a good agreement with the SNR emission shown in the DSS2 image.

Group III spectra exhibit emission lines of which the origin is unclear. When several emission lines not usually seen in stellar spectra are marginally detected, these spectra are classified into this group. In some cases, Group III spectra show a few strong emission lines such as Hα, [S II] $\lambda\lambda$6717,6731, or [O III] λ5007. However, they do not have high [S II]/Hα ratios, which is often used as a diagnostic of SNR origin (e.g., see McKee & Hollenbach 1980; Fesen et al. 1985; Long 1985), or this ratio cannot be measured properly because the Hα or [S II] lines (or both) are contaminated or do not appear. Moreover, their spatial correspondences to the SNR emission shown in the DSS2 image are not often discernible. Ambiguity of their association is partially due to lack of narrowband images (e.g., Hα image). The presence of Balmer-dominated filaments from nonradiative shocks in the Cygnus Loop is well known (e.g., Raymond et al. 1983; Fesen et al. 1985; Long et al. 1992; Hester et al. 1994; Sankrit et al. 2000; Ghavamian et al. 2001; Blair et al. 2005; Medina et al. 2014; Katsuda et al. 2016), but these filaments are usually fainter than emission from radiative shocks. Since faint Balmer-dominated filaments may not be distinct in the DSS2 red image, it is currently inconclusive whether those showing Balmer lines only in Group III originate from the Cygnus Loop. For example, a spectrum of obs. ID 470509056 presents a weak Hα line only (see Figure 2). This spectrum might be related to one of Balmer-dominated filaments, but its location (α_{J2000}, δ_{J2000}) = (20:57:39.9, +30:40:05.7), relatively far away from the bright filaments, requires further verification. Likewise, no prominent lines except for [O III] $\lambda\lambda$4959,5007 (and weak [O II] λ3727) are found in several Group III spectra, which are most likely associated with the SNR, too. For example, the spectrum of obs. ID 470516196 shows (see the zoomed-in spectrum near Hα in Figure 2) the presence of weak absorption at the wavelengths of [S II] (and [N II]), which implies that several emission lines from the SNR are oversubtracted during the removal of night sky lines. There are 176 spectra in this category, and most of them are located in the vicinity of the bright filaments or diffuse interior (see the spatial distribution of black circles in Figure 1). This suggests that Group III spectra are likely to be associated with the SNR, and further investigation will clarify their origin.

Group IV is for stellar-emission-only spectra. Two-hundred thirty-four spectra are classified based on no evidence for any association to the SNR. Figure 1 shows that Group IV spectra (yellow circles) are uniformly distributed over the entire remnant in general, which supports their nonassociation with the SNR.

2.2. Line Identification

For Group I and II, line identification is carried out to measure line intensities and to derive relative ratios. Those with high S/Ns clearly exhibit various emission lines as previously reported (e.g., Fesen et al. 1982; Fesen & Hurford 1996): [O II] λ3727, [Ne III] λ3869, [S II] $\lambda\lambda$4069, 4076, [O III] λ4363, [Fe III] λ4658, He II λ4686, [O III] $\lambda\lambda$4959, 5007, [N I] λ5200, [N II] λ5755, He I λ5876, [O I] $\lambda\lambda$6300, 6364, [N II] $\lambda\lambda$6548, 6583, [S II] $\lambda\lambda$6717, 6731, [Ca II] $\lambda\lambda$7291, 7324, [O II] $\lambda\lambda$7320, 7330, and the Balmer lines (e.g., Hα, Hβ, Hγ, etc.).[8] Various weak lines are also detected including [Fe II] λ4359, [Fe III] λ4986, [Fe II] λ5158, [S III] λ6312, He I λ7065, [Ar III] λ7136, [Fe II] λ7155, He I λ7281, and [Ni II] λ7378. To handle bulk data consistently and efficiently, we do not aim to fit every detected line, only fitting those needed for further analysis. Consequently, intensities of 15 emission lines (i.e., [O II] λ3727, [Ne III], [O III] λ4363, Hβ, [O III] λ4959+, [N I], [N II] λ5755, [O I] λ6300+, [N II] λ6548+, Hα, and [S II] λ6717+) are obtained for Groups I and IIa, and only [S II] λ6717+ are obtained for Group IIb.

For Group I spectra (i.e., SNR-dominated spectra), line intensities are measured by a Gaussian fit with a linear baseline to each line profile. When two or more emission lines are adjacent, such as Hα and [N II] λ6548+ or [S II] λ6717+, a

[8] Unless otherwise specified, [Ne III] λ3869, [O III] $\lambda\lambda$4959, 5007, [N I] λ5200, [O I] $\lambda\lambda$6300, 6364, [N II] $\lambda\lambda$6548, 6583, and [S II] $\lambda\lambda$6717, 6731 are shortly [Ne III], [O III] λ4959+, [N I], [O I] λ6300+, [N II] λ6548+, and [S II] λ6717+, respectively.

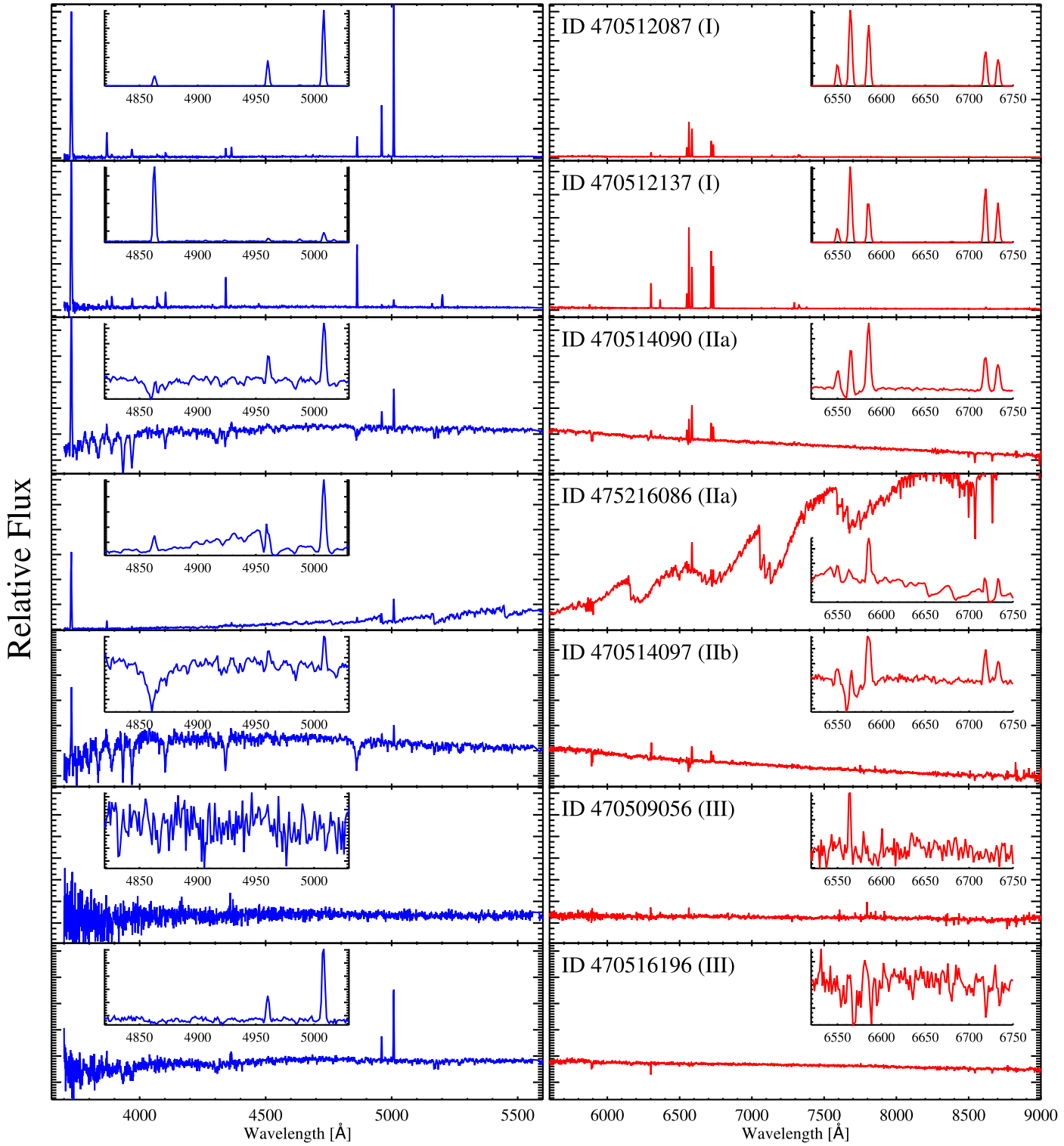

Figure 2. Exemplary LAMOST spectra of Groups I, IIa, IIb, and III. The blue and red spectra are shown in left and right panels, respectively. Obs ID with its spectral group in parenthesis (see Table 2) is marked in the right panel. In each panel, its zoomed-in spectrum near Hβ or Hα is displayed. The first and second spectra from the top are representative of SNR-dominated Group I spectra with high and low [O III]/Hβ ratios, respectively. The two Group IIa spectra clearly show both SNR-related emission and stellar features. Superposed stars are likely to be F and M types (third and fourth rows, respectively). A spectrum in Group IIb (fifth row) exhibits some emission lines with strong absorption features. Two Group III spectra show limited sets of emission lines, and their origins are inconclusive. While only the Hα line appears in obs. ID 470509056 spectrum (sixth row), [O III] lines with weak [O II] λ3727 are present in obs. ID 470516196 spectrum (bottom row).

single baseline from a wider wavelength range is used for all of these lines. Integrated intensities normalized to Hβ are listed in Table 3. Although LAMOST sky subtraction using principal component analysis reduces the averages of residuals down to $\sim$3% (Bai et al. 2017), several emission lines, especially weak lines, could still be contaminated by the residuals. For instance, relatively weak [O III] λ4363 might be affected by Hg line at 4358 Å arising from mercury streetlights, and [O I] λ6300+

Table 3
Relative Line Intensities for Group I Spectra Relative to Hβ (Hβ = 100)

Obs. ID	[O II] λ3727	[Ne III] λ3869	[O III] λ4363	[O III] λ4959	[O III] λ5007	[N I] λ5200	[N II] λ5755	[O I] λ6300	[O I] λ6364	[N II] λ6548	Hα λ6564	[N II] λ6583	[S II] λ6717	[S II] λ6731	Hβ Flux[a] (counts)
470503073	2550	158	⋯	142	486	⋯	⋯	84	⋯	142	272	462	239	191	306 ± 58
470503103	2725	137	63	202	650	⋯	⋯	76	24	146	483	441	234	213	220 ± 37
470503109	1212	64	22	59	175	8	5	55	15	52	275	167	264	240	1833 ± 189
470503144	785	34	⋯	26	95	14	⋯	64	18	69	318	222	121	97	734 ± 84
470503149	707	⋯	⋯	24	⋯	29	⋯	251	59	63	406	213	79	60	154 ± 20
470503216	2260	214	84	342	1077	⋯	11	18	3	103	290	325	192	139	1297 ± 143
470504035	1338	83	34	110	321	15	⋯	69	20	70	301	240	262	190	172 ± 19
470504061	1056	89	37	126	394	⋯	7	16	6	28	264	98	61	45	409 ± 43
470504132	1026	⋯	⋯	⋯	34	31	⋯	142	48	66	237	202	178	130	345 ± 36
470504139	1314	165	78	313	936	⋯	⋯	45	16	36	345	126	116	86	202 ± 22
470504144	1125	63	18	76	213	4	5	36	12	59	305	180	117	85	878 ± 88
470504151	1105	⋯	⋯	13	30	32	⋯	150	51	67	306	235	267	203	272 ± 29
470505053	726	⋯	⋯	68	239	27	⋯	108	49	72	440	258	181	136	166 ± 19
470509027	2123	245	127	445	1377	⋯	⋯	29	5	79	320	281	192	153	940 ± 101
470509075	1275	79	⋯	64	221	⋯	⋯	56	14	81	299	230	188	159	311 ± 34
470509080	556	13	⋯	9	28	34	⋯	115	36	58	328	196	144	119	1462 ± 149
470509089	2170	178	90	284	777	⋯	⋯	111	23	119	337	336	175	147	251 ± 30
470509097	1129	55	23	64	218	16	⋯	61	14	69	268	222	160	125	2344 ± 240
470509098	861	270	162	535	1558	⋯	⋯	105	28	40	397	99	44	34	117 ± 15
470511036	2296	156	54	153	488	34	9	153	51	161	514	567	367	276	1411 ± 163
470511039	786	19	⋯	17	60	16	⋯	85	26	63	282	197	174	132	1149 ± 117
470511109	790	22	3	13	41	31	5	124	40	79	346	216	188	138	2031 ± 203
470511160	1048	39	9	32	108	14	5	73	17	74	285	268	193	154	1341 ± 141
470511161	926	40	⋯	46	160	18	6	92	14	74	286	250	180	136	758 ± 81
470511167	762	38	⋯	36	116	14	⋯	56	13	87	345	274	217	161	642 ± 66
470511185	1725	⋯	⋯	58	221	⋯	⋯	220	54	138	359	445	262	198	78 ± 13
470511201	845	⋯	⋯	11	36	27	⋯	195	51	111	344	375	135	104	263 ± 29
470511223	1700	⋯	⋯	132	307	⋯	⋯	155	74	124	292	350	177	133	97 ± 14
470512067	1116	64	⋯	54	153	⋯	⋯	52	16	74	265	224	143	108	191 ± 21
470512069	868	48	13	45	137	14	4	62	17	70	268	217	172	134	1450 ± 146
470512080	1001	81	31	106	319	18	5	77	25	73	279	243	182	139	1252 ± 126
470512083	1029	124	42	166	482	⋯	⋯	7	7	78	460	284	194	154	162 ± 19
470512084	1808	179	60	208	612	12	10	82	22	109	344	355	245	203	1899 ± 219
470512087	1406	152	54	240	735	5	6	33	9	71	263	209	118	93	1002 ± 100
470512129	1585	197	70	227	670	⋯	⋯	34	9	70	245	206	122	98	195 ± 21
470512135	798	⋯	⋯	114	278	⋯	⋯	30	12	20	202	70	44	42	52 ± 7
470512137	438	16	⋯	3	11	31	3	63	20	33	179	103	129	90	1585 ± 159
470512241	1263	186	75	291	884	9	6	25	2	53	302	192	146	116	881 ± 92
470514093	1778	128	39	190	561	18	6	79	15	112	309	352	237	177	888 ± 97
470514094	1563	100	41	116	369	19	4	85	21	99	305	303	157	119	1048 ± 110
470514096	1122	107	42	184	549	⋯	5	19	6	52	229	168	111	120	425 ± 43
470514141	1140	⋯	72	210	632	21	⋯	44	10	50	309	197	121	79	148 ± 17
470514142	1632	120	36	146	445	11	6	45	12	78	287	298	144	106	2024 ± 205
470514165	2973	377	174	642	1910	⋯	11	23	3	59	324	247	123	97	741 ± 77
470514168	1379	68	19	81	233	12	3	52	13	65	282	258	143	107	1159 ± 116
470515006	2625	158	76	243	753	⋯	⋯	31	⋯	91	257	246	198	194	228 ± 42
470515065	3939	⋯	⋯	146	473	⋯	⋯	120	65	194	531	679	277	206	48 ± 10

Table 3
(Continued)

Obs. ID	[O II] λ3727	[Ne III] λ3869	[O III] λ4363	[O III] λ4959	[O III] λ5007	[N I] λ5200	[N II] λ5755	[O I] λ6300	[O I] λ6364	[N II] λ6548	Hα λ6564	[N II] λ6583	[S II] λ6717	[S II] λ6731	Hβ Flux[a] (counts)
470515199	2253	148	80	210	709	⋯	⋯	⋯	⋯	49	425	188	105	92	113 ± 19
470516089	948	38	14	44	125	40	⋯	128	36	69	271	232	196	153	1876 ± 195
470516108	⋯	⋯	85	192	586	⋯	⋯	50	⋯	⋯	343	⋯	19	⋯	46 ± 10
470516172	811	⋯	⋯	⋯	44	8	⋯	33	20	60	320	202	185	125	300 ± 31
470516174	1337	64	12	49	159	20	8	85	24	84	322	269	191	143	630 ± 66
470516184	1813	⋯	⋯	⋯	296	⋯	⋯	87	⋯	83	404	314	389	281	49 ± 11
470516229	1271	74	16	78	238	14	5	69	18	67	280	257	209	175	1131 ± 114
470516246	1740	126	34	169	516	8	7	30	8	64	226	231	111	83	1271 ± 128
475203151	2148	91	⋯	91	336	135	⋯	336	69	270	517	878	367	283	1065 ± 164
475211039	948	43	⋯	51	149	11	⋯	139	43	118	625	470	230	244	1558 ± 166
475211106	562	19	2	13	45	14	3	86	27	63	331	294	100	322	5080 ± 510
475211136	1667	76	41	216	282	21	⋯	192	48	160	519	492	214	167	1203 ± 131
475211152	1360	67	15	96	313	⋯	9	24	12	110	412	366	291	224	1275 ± 140
475211160	954	19	⋯	43	146	28	⋯	164	57	128	502	420	296	236	1065 ± 119
475211213	1432	⋯	⋯	⋯	171	⋯	⋯	97	28	103	440	310	279	201	214 ± 50
475212060	1106	⋯	⋯	86	206	⋯	⋯	26	10	58	210	182	64	55	125 ± 24
475212080	1651	150	53	296	919	10	6	38	8	104	305	322	247	203	5351 ± 555
475212129	789	31	⋯	41	130	⋯	⋯	38	5	48	252	153	162	122	576 ± 60
475212236	1318	65	50	102	306	45	⋯	124	18	121	431	355	276	237	3264 ± 494
475214088	1502	117	56	180	727	⋯	⋯	50	⋯	143	354	694	340	243	1800 ± 247
475214135	683	⋯	⋯	16	42	29	⋯	252	75	146	365	342	246	169	977 ± 100
475215159	673	25	8	50	177	24	⋯	138	38	81	419	254	132	97	781 ± 82
475215190	1632	235	109	526	1674	⋯	⋯	279	⋯	37	545	165	60	⋯	66 ± 18
475216143	862	46	8	62	211	30	8	103	34	95	300	309	235	161	2308 ± 233
475216147	717	37	7	29	97	55	7	139	44	81	374	257	228	172	3106 ± 49
475216228	2404	179	⋯	112	408	⋯	⋯	144	49	196	440	598	269	214	301 ± 47
475216229	1236	155	32	110	383	⋯	⋯	226	68	159	425	441	331	254	393 ± 49
475216241	708	33	⋯	⋯	39	16	⋯	123	40	117	429	341	239	177	976 ± 105

Notes. Ellipses indicate nondetection.

[a] Note that the Hβ flux quoted here does not necessarily represent the absolute brightness at the position of a given fiber since the LAMOST spectra are not absolute-calibrated (see Section 2.1). However, it is worthwhile to list them because the flux with uncertainty gives an idea for the S/N of the entire spectrum to some extent. The final uncertainty is the quadratic sum of the calibration errors (10% adopted) and the flux uncertainties mainly arising fluctuation of the baseline during a linear fitting (see Section 2.2).

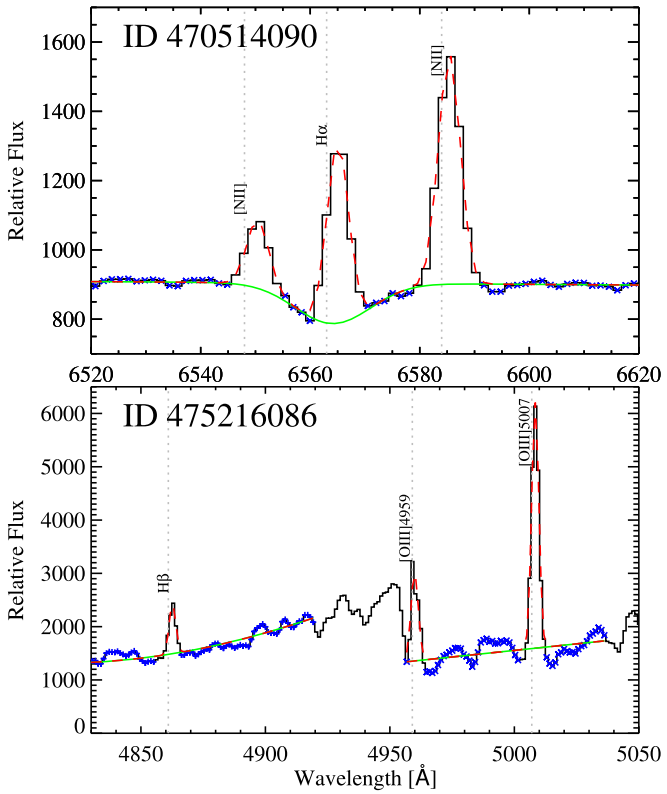

Figure 3. Example line-fitting results for Group IIa spectra that require additional treatment (see details in Section 2.2). Obs. ID 470514090 spectrum near Hα and obs. ID 475216086 near Hβ (both also shown in Figure 2) are presented in the upper and lower panels, respectively. Each plot shows the spectrum in black, the full best-fit model in red, and the baseline in green. Data points used for the baseline fit are marked with blue "x" symbols. For obs. ID 475216086, [O III] λ4959, 5007 share their baseline, which is determined with a linear fitting around the selected wavelength range. Because the continuum near [O III] λ4959 is affected by TiO bands, the baseline only includes its redward range.

can be contaminated by imperfect subtraction of the strong [O I] night sky emission. When the determination of the baseline is problematic or the emission feature is damaged, only upper limits are quoted.

For Group IIa spectra (i.e., SNR+stellar spectra), most of line intensities are measured in the same way as those for Group I. When hydrogen absorption is significant or other stellar features contaminate the neighborhood of an emission line, however, additional treatment is applied (see examples in Figure 3). For Hα or Hβ lying on top of a stellar absorption feature, the absorption feature is first fitted with a negative Gaussian (or a Lorentz profile for some cases with a wider wing). For instance, Obs. ID 470514090 shows a series of H absorption features, which is fitted by a negative Gaussian (green line in Figure 3). Then, the fitted absorption profile is used as a baseline to fit the emission line from the SNR. Also, when the star along the line of sight is an M type, TiO bands can dominate its spectrum. In such cases, [O III] λ4959 is adjacent to one of TiO bands (e.g., see obs. ID 475216086 in Figure 3), so we only use its redward range (marked with blue "x" in Figure 3) for baseline fitting. Measured line intensities relative to Hβ for Group IIa spectra are listed in Table 4.

In spite of the 10% precision expected for high-S/N spectra (Xiang et al. 2015, see also Section 2.1), note that there are indications of larger errors in some spectra. The Balmer decrements, Hα/Hβ, should be close to 2.9 in the recombining plasma of SNR shocks (Hummer & Storey 1987), and the typical reddening to the Cygnus Loop $E(B-V)$ (Fesen et al. 2018) would increase that ratio to 3.1–3.2. Spectra in Tables 3–4 below span the range from 2.02 to 6.25. Relatively slow shocks in partly neutral gas can produce higher Balmer decrements (Raymond 1979), but the high [O III]/Hβ ratios of those spectra show that they are not such slow shocks. A higher reddening could account for some of the spectra with large Balmer decrements, and the western limb of the Cygnus Loop shows the interaction of the shock with a dense cloud having $E(B-V)$ up to about 0.5 (Fesen et al. 2018), but even that would not account for Balmer decrements above 4. We conclude that some of the measured Balmer line ratios are erroneous by factors of 1.5 or more. This might be an offset between the red and blue sections of the spectra, but there is no obvious correlation between Balmer decrements and ratios between other lines at the red and blue ends of the spectrum. We therefore caution that the uncertainties are larger than might have been expected, and those with Hα/Hβ < 2.9 or >4.0 are denoted with open symbols in Figures 4–8.

3. Results

3.1. Variations and Correlations of Line Ratios

For the 154 Group I and IIa spectra in total, we measure line intensities relative to Hβ. To the best of our knowledge, this is the largest sample of optical spectra with line measurement observed in the Cygnus Loop, which does not just focus on bright filaments but covers all regions of the SNR. As listed in Tables 3 and 4 and presented in the sample spectra in Figure 2, the relative strengths of line emission vary significantly at different positions within the Cygnus Loop, and correlations among line ratios of different elements or different transitions are observed. As previously noticed (e.g., Fesen et al. 1982, hereafter, F82), the intensity of [O III] λ4959+ relative to Hβ varies over two orders of magnitude (from 0.15 to $\gtrsim$25 in Group I), and other lines such as [O II] λ3727, [N II] λ6548+, and [S II] λ6717+ also vary in intensity over an order of magnitude, suggesting the presence of diverse physical conditions inside the single remnant. Note that dereddening is not applied here since the LAMOST spectra are only relatively flux calibrated (Section 2.1). However, as extinction to the remnant is relatively low (e.g., $E(B-V) = 0.08$ mag, Parker 1967), we postulate this does not affect our results significantly, in particular, when we compare emission lines nearby. To demonstrate the effect of extinction, line ratios using measured intensities and those of dereddened intensities in F82 are overplotted as a reference (see Figures 4–8).

3.1.1. Line Ratios of Different Elements

Systematic correlations appear between line ratios of different elements, especially with the same ionization state. For example, those with a high-ionization state such as [Ne III] and [O III] λ4959+ show a tight correlation (correlation coefficient[9] of $R = 0.90$) with each other (Figure 4(a)). This is a natural consequence of the fact that lines from high-ionization species tend to be strong where lines from other elements with high ionization are strong. Similarly, close correlations of [N I] with [O I] λ6300+ and [N II] λ6548+ with

[9] Note that the line ratios from F82 are not included for deriving the correlation coefficients shown in Figures 4–6.

Table 4
Relative Line Intensities for Group IIa Spectra Relative to Hβ (Hβ = 100)

Obs. ID	[O II] λ3727	[Ne III] λ3869	[O III] λ4363	[O III] λ4959	[O III] λ5007	[N I] λ5200	[N II] λ5755	[O I] λ6300	[O I] λ6364	[N II] λ6548	Hα λ6564	[N II] λ6583	[S II] λ6717	[S II] λ6731	Hβ flux[a] (counts)
470503207	927	⋯	⋯	⋯	101	⋯	⋯	41	⋯	65	507	190	42	59	500 ± 110
470504019	1617	⋯	⋯	27	88	72	⋯	175	25	172	344	571	242	212	411 ± 60
470504066	1979	120	53	104	337	⋯	8	6	⋯	51	239	184	107	91	281 ± 39
470509065	1306	72	⋯	⋯	92	⋯	⋯	90	⋯	90	337	320	260	222	293 ± 56
470511206	1196	⋯	⋯	⋯	279	⋯	⋯	95	⋯	45	235	186	98	95	26 ± 11
470512054	⋯	⋯	⋯	46	123	⋯	⋯	35	7	6	281	39	⋯	⋯	124 ± 16
470512145	⋯	⋯	⋯	42	105	⋯	⋯	91	34	20	160	55	30	42	27 ± 6
470514079	3450	110	⋯	119	380	⋯	⋯	338	⋯	328	496	1011	381	360	249 ± 102
470514157	410	47	28	67	208	⋯	⋯	12	4	9	308	42	28	28	433 ± 51
470515071	972	⋯	⋯	56	252	⋯	⋯	64	⋯	65	453	217	125	115	88 ± 23
470515072	1360	87	⋯	⋯	⋯	40	⋯	94	⋯	120	288	319	246	196	98 ± 14
470515095	1051	⋯	⋯	⋯	40	⋯	⋯	37	⋯	62	266	200	151	127	118 ± 18
470516241	2274	82	⋯	93	228	⋯	⋯	72	⋯	148	325	434	283	236	739 ± 146
475209098	530	⋯	⋯	55	176	⋯	⋯	38	9	28	197	99	72	55	305 ± 40
475211030	1372	40	⋯	61	230	⋯	⋯	63	⋯	135	699	432	278	252	2009 ± 394
475211036	3571	150	⋯	273	835	⋯	⋯	240	⋯	304	794	1031	756	708	1138 ± 503
475214165	4116	435	272	1069	2288	⋯	⋯	⋯	⋯	301	382	1012	359	577	762 ± 286
470503118	2992	206	62	283	852	⋯	⋯	48	17	106	322	338	292	214	444 ± 46
470503142	1294	91	55	133	379	⋯	13	103	⋯	108	319	333	153	160	284 ± 44
470503172	1622	62	⋯	54	264	⋯	⋯	62	⋯	85	312	308	196	175	433 ± 71
470503215	922	54	⋯	⋯	82	⋯	⋯	176	43	124	326	358	173	124	313 ± 73
470504022	845	⋯	⋯	⋯	92	79	⋯	230	78	160	244	443	112	82	92 ± 19
470504194	1085	⋯	⋯	58	203	⋯	⋯	⋯	⋯	40	515	173	46	98	467 ± 135
470505067	2997	131	116	216	748	79	⋯	149	⋯	227	552	630	537	455	378 ± 112
470509055	1847	174	⋯	145	474	⋯	⋯	104	24	78	281	242	195	155	141 ± 18
470509084	1185	35	⋯	88	255	18	15	34	⋯	63	240	184	183	163	222 ± 36
470511031	1699	130	47	154	469	24	8	80	26	91	361	291	159	118	1870 ± 189
470511035	743	54	⋯	13	77	⋯	⋯	72	20	47	440	161	30	28	339 ± 37
470511037	1317	57	⋯	25	103	26	⋯	126	39	105	309	323	189	146	1594 ± 161
470511124	2027	⋯	⋯	26	125	⋯	⋯	233	54	152	506	532	324	245	79 ± 19
470511144	1395	⋯	⋯	⋯	⋯	98	⋯	363	120	180	314	548	233	176	170 ± 23
470511154	908	⋯	⋯	⋯	92	⋯	⋯	74	44	67	442	275	228	179	111 ± 22
470511157	2648	⋯	⋯	⋯	365	⋯	⋯	200	35	205	757	766	575	475	108 ± 23
470512051	819	64	21	55	172	31	3	103	34	77	333	240	197	152	1484 ± 150
470512052	963	59	15	40	115	31	3	112	37	65	309	249	232	176	949 ± 96
470512058	964	73	19	51	150	34	5	123	40	97	326	298	250	182	906 ± 91
470512064	978	231	⋯	221	929	⋯	⋯	81	⋯	36	675	158	69	95	80 ± 21
470512068	798	191	132	331	928	⋯	⋯	419	⋯	50	319	141	69	58	455 ± 96
470512072	1434	167	⋯	56	190	⋯	⋯	90	22	93	280	314	229	178	333 ± 65
470512073	1469	85	⋯	46	203	⋯	⋯	88	9	123	415	389	329	265	571 ± 104
470512079	1571	171	102	207	591	30	⋯	77	22	151	450	397	335	286	249 ± 45
470512099	1533	⋯	⋯	423	1237	⋯	⋯	55	⋯	108	787	420	180	220	20 ± 7
470512147	846	91	⋯	59	180	⋯	⋯	35	⋯	67	315	211	259	205	353 ± 46
470512236	1145	⋯	⋯	58	147	⋯	⋯	74	⋯	97	335	312	149	139	219 ± 57
470514081	732	⋯	⋯	50	86	⋯	⋯	146	23	113	272	222	202	149	46 ± 9
470514085	1382	124	58	225	656	⋯	⋯	35	7	76	310	268	233	171	252 ± 28
470514087	980	⋯	⋯	31	100	⋯	128	⋯	⋯	167	251	298	⋯	⋯	213 ± 35

Table 4
(Continued)

Obs. ID	[O II] λ3727	[Ne III] λ3869	[O III] λ4363	[O III] λ4959	[O III] λ5007	[N I] λ5200	[N II] λ5755	[O I] λ6300	[O I] λ6364	[N II] λ6548	Hα λ6564	[N II] λ6583	[S II] λ6717	[S II] λ6731	Hβ flux[a] (counts)
470514089	1461	91	30	123	291	…	15	…	…	102	400	347	137	153	602 ± 73
470514090	2655	271	118	166	497	42	…	164	51	176	456	588	319	255	567 ± 89
470515085	1067	…	…	53	166	…	17	170	39	66	478	227	177	133	115 ± 18
470515187	2537	…	…	57	215	…	…	188	53	71	357	312	261	192	27 ± 7
470515213	1759	…	…	63	254	…	…	…	…	70	155	236	140	121	201 ± 28
470516034	2530	325	281	553	1340	…	…	21	…	52	244	217	173	123	66 ± 8
470516054	2414	61	50	72	219	23	11	68	17	123	361	389	267	203	687 ± 87
470516057	1090	60	24	63	180	11	6	58	19	63	253	212	171	127	844 ± 86
470516065	849	…	…	…	…	41	…	117	27	78	296	242	196	154	462 ± 60
470516083	1551	129	…	88	337	…	…	93	19	68	454	227	152	130	347 ± 57
470516084	2619	121	…	132	436	…	…	86	…	128	323	348	279	251	272 ± 49
470516085	1738	88	…	…	45	27	…	108	38	121	343	403	211	167	180 ± 24
470516086	2362	207	39	203	642	…	…	28	5	105	392	338	255	197	261 ± 31
470516140	2215	89	…	86	241	…	…	85	…	137	285	419	170	136	522 ± 74
470516144	2105	120	…	84	326	…	…	26	…	126	328	390	213	175	410 ± 58
470516147	771	47	…	22	78	37	2	129	33	71	286	210	155	114	927 ± 96
470516194	1938	86	…	26	119	…	…	107	…	153	432	446	294	271	293 ± 52
470516231	1479	…	…	59	214	15	15	122	49	137	426	474	308	230	253 ± 28
470516239	1658	96	49	179	622	26	…	30	17	107	401	397	216	171	256 ± 38
470516248	3001	509	307	633	1879	…	…	37	…	107	725	413	177	155	156 ± 29
475204144	1381	…	…	49	187	53	6	174	51	102	418	358	236	178	404 ± 60
475211020	958	…	…	…	241	…	…	…	30	141	502	396	430	312	133 ± 28
475211201	671	…	…	57	146	…	…	86	15	60	275	171	126	117	900 ± 140
475211223	1328	…	…	130	316	…	…	153	41	108	306	286	156	123	238 ± 71
475212052	2165	…	…	103	242	…	…	207	…	252	626	776	502	473	318 ± 123
475212135	1283	…	…	145	465	…	…	45	…	123	477	389	387	322	172 ± 39
475214211	1216	…	84	190	554	14	…	100	43	109	533	393	191	136	537 ± 76
475215061	2714	…	…	42	139	…	…	150	…	243	330	723	371	338	272 ± 83
475216063	776	…	…	68	229	81	…	191	56	100	443	349	358	292	2778 ± 341
475216066	1654	…	…	45	214	…	…	198	69	182	556	626	671	381	361 ± 50
475216086	1988	164	69	197	527	…	153	…	…	173	133	869	240	255	3126 ± 511
475216246	1232	81	9	52	147	18	9	100	33	92	261	271	167	134	2173 ± 226

Notes. Ellipses indicate nondetection.
[a] Same as Table 3.

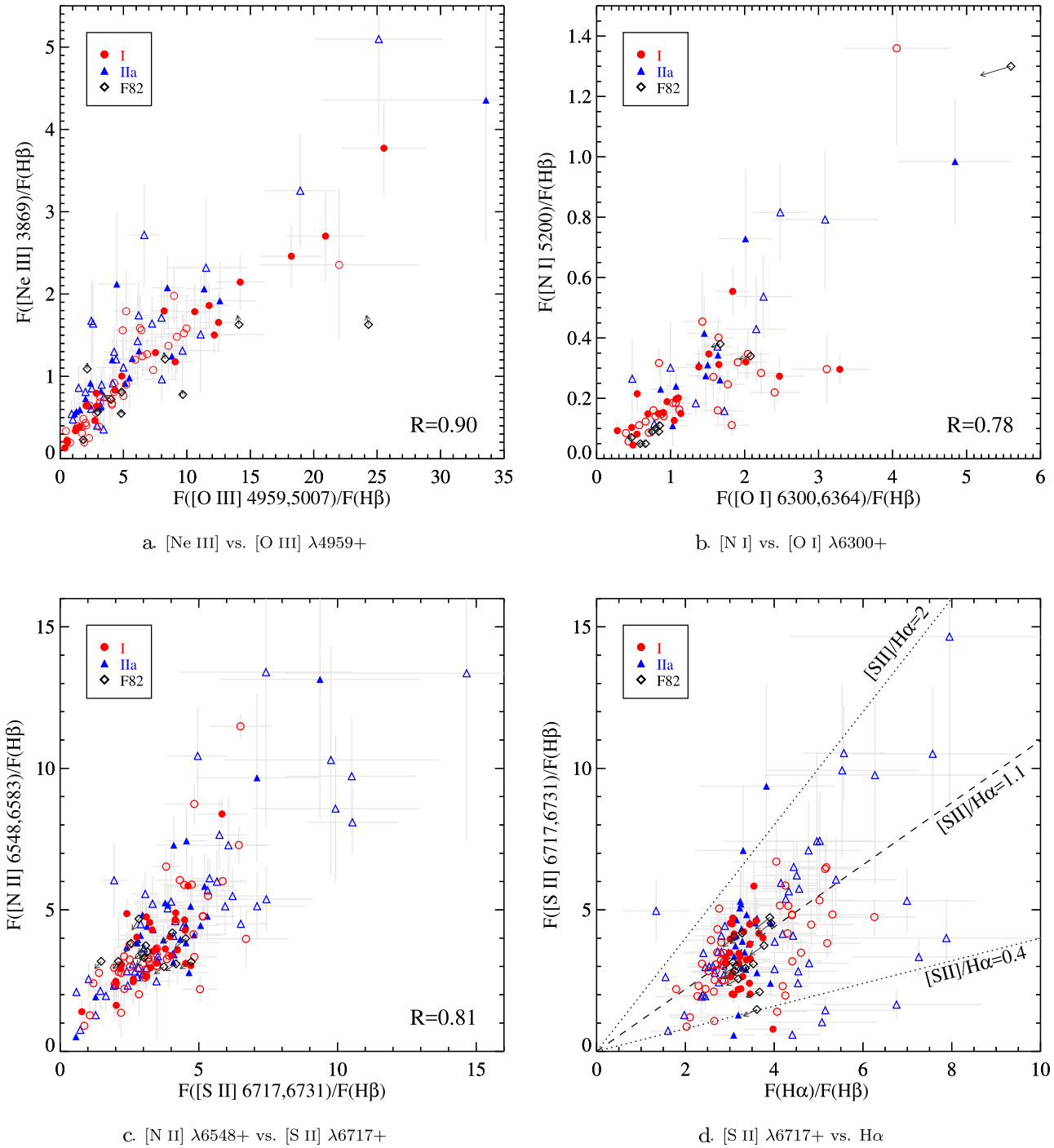

a. [Ne III] vs. [O III] λ4959+

b. [N I] vs. [O I] λ6300+

c. [N II] λ6548+ vs. [S II] λ6717+

d. [S II] λ6717+ vs. Hα

Figure 4. Correlation between line ratios of different elements: Panel (a): [Ne III] vs. [O III] λ4959+; panel (b): [N I] vs. [O I] λ6300+; panel (c): [N II] λ6548+ vs. [S II] λ6717+; and panel (d): [S II] λ6717+ vs. Hα. All line intensities are normalized to Hβ. Group I and IIa spectra are denoted with circles and triangles, respectively. Those with Hα/Hβ < 2.9 or > 4.0 are denoted with open symbols while the rest are marked with filled symbols (see the text). For comparison, (measured) line ratios from F82 are overlaid with diamonds, and the effect of dereddening is marked with arrows. Hereafter, the symbol designation is applied in the same way as for Figures 5–8. For the correlations shown in panels (a)–(c), the correlation coefficients (*R*) are measured for Groups I and IIa (those from F82 excluded). In panel (d), a commonly used shock diagnostic, [S II] λ6717+/Hα, is denoted. In most cases, [S II] λ6717+/Hα ranges between 0.4 and 2.0 (dotted lines), and the median ratio from our measurement is ∼1.1 (dashed line).

[S II] λ6717+ are also present (Figures 4(b) and (c)). Where low-ionization or neutral species emit strongly, lines from other low-ionization species appear to be strong, while lines from high-ionization species become weaker.

The ratio of [S II] λ6717+/Hα is a well-known shock diagnostic (e.g., Mathewson & Clarke 1973): a high [S II] λ6717 +/Hα ratio (i.e., ≳0.4) indicates SNRs whereas a low ratio (often ∼0.1) indicates H II regions. In Figure 4(d), the intensity of [S II] λ6717+ is compared with the Hα intensity. Except for a few points, the [S II] λ6717+/Hα ratios measured from the Group I and IIa spectra well exceed 0.4, corroborating the SNR origin. The observed ratios mostly range between 0.4 and 2.0 (between dotted lines in Figure 4(d)), and the median is ∼1.1 (dashed line). Besides those with [S II] λ6717+/Hα ⩾ 0.4,

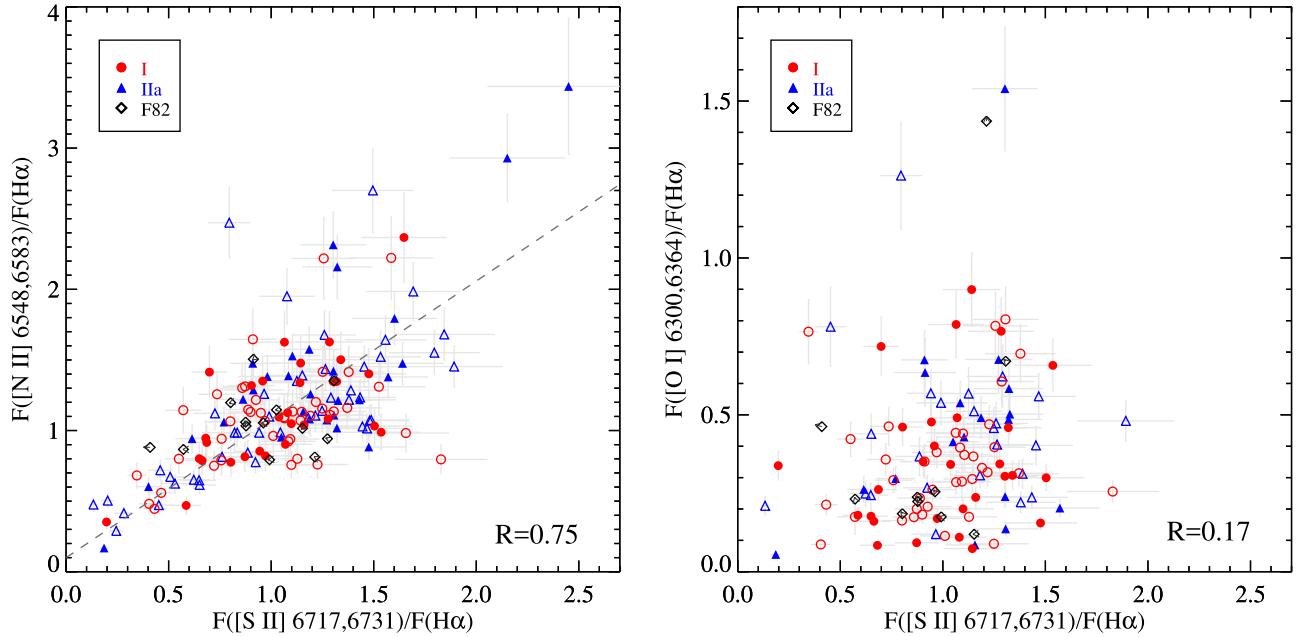

Figure 5. Shock diagnostic [S II] λ6717+/Hα ratios in comparison with [N II] λ6548+/Hα (left panel) and [O I] λ6300+/Hα (right panel). While [N II] λ6548+/Hα has a good correlation with [S II] λ6717+/Hα (correlation coefficient $R = 0.75$), [O I] λ6300+/Hα shows no obvious evidence of correlation with [S II] λ6717+/Hα ($R = 0.17$). For the correlation between [N II] λ6548+/Hα and [S II] λ6717+/Hα, a linear fit is given with a dashed line ($y = a + bx$ where $a = 0.10 \pm 0.04$ and $b = 0.98 \pm 0.03$).

there are 10 spectra (4 Group I and 6 Group IIa) showing significantly weak [S II] λ6717+ emission relative to Hα (i.e., $0.13 \lesssim$ [S II] λ6717+/H$\alpha \lesssim 0.34$). Half of them are along the interior filaments (like position H of F82), four are located at the outskirts of the bright NE region NGC 6992, and one is near the bright SW region NGC 6960. These spectra show either strong [O I] λ6300+ and/or [O II] λ3727 line emission or high [O III] λ4959+/Hβ ratio, or both. Because of their locations as well as their spectral features, their emission is probably associated with the Cygnus Loop.

We compare [N II] λ6548+/Hα and [O I] λ6300+/Hα ratios with respect to [S II] λ6717+/Hα in Figure 5, which are previously known to correlate, especially for extragalactic SNRs (e.g., Smith et al. 1993; Gordon et al. 1998; Lee et al. 2015; Long et al. 2018). The [N II] λ6548+/Hα ratios of the Cygnus Loop show a fairly good correlation with the [S II] λ6717+/Hα ratios ($R \simeq 0.75$), verifying it as the secondary shock indicator. A linear fit to the correlation is performed, which gives [N II] λ6548+/H$\alpha = (0.10 \pm 0.04) + (0.98 \pm 0.03) \times$ [S II] λ6717+/Hα (dashed line in Figure 5 (left panel)). On the other hand, [O I] λ6300+/Hα shows no evidence for correlation with [S II] λ6717+/Hα ($R = 0.17$, see Figure 5 (right panel)). This is somewhat surprising because [O I] λ6300+ lines are considered to be a useful discriminant for shock-heated gas, and this ratio shows a good correlation with [S II] λ6717+/Hα as [N II] λ6548+/Hα for extragalactic SNRs (e.g., Gordon et al. 1998, see also Lee et al. 2015). We attribute the lack of correlation partly to observational difficulties because the [O I] emission from the night sky can contaminate the LAMOST spectra, especially those with low S/Ns (see Tables 3–4). However, the correlation is not apparent in the samples of F82, either. Also, the correlation appears weak for SNRs in some other galaxies (see Figure 11 of Lee et al. 2015). Thus, the correlation between [O I] λ6300+/Hα and [S II] λ6717+/Hα may be limited to radiative SNRs with bright optical emission lines and needs a more careful investigation.

3.1.2. Line Ratios of Different Transitions

In Figure 6, we examine line ratios of the same element such as oxygen or nitrogen with different transitions. The largest variation among all possible combination of line ratios is seen in the intensities of [O II] λ3727 and [O III] λ4959+ emission relative to Hβ, which range from $\sim$0.15 to $\sim$40. Such a large span clearly depicts the diversity of physical conditions within the Cygnus Loop (e.g., Fesen et al. 1982; Levenson et al. 1998). As previously reported in F82, we also note that the ratio of [O II] λ3727/Hβ is no less than $\sim$4 in any case (see Figures 6(a) and (b)), whereas both [O I] λ6300+/Hβ and [O III] λ4959+/Hβ can be as low as $\sim$0.15. This distinction of the [O II] λ3727/Hβ ratios (i.e., [O II] λ3727/H$\beta \gtrsim 4$) has been seen in other Galactic SNRs as well as extragalactic SNRs (e.g., see Figures 3 and 4 of Fesen et al. 1985), which can be used to separate SNRs from H II regions.

The intensities of [O II] λ3727 and [O III] λ4959+ relative to Hβ appear to correlate moderately ($R = 0.54$, Figure 6(a)) whereas [O II] λ3727 and [O I] λ6300+ do not show an apparent correlation (Figure 6(b)). However, as guided by the data from F82 (diamonds in Figure 6(b)), the general trend would exist in a way that the [O II] λ3727/Hβ ratios tend to decrease as the [O I] λ6300+/Hβ ratios increase.

For nitrogen, the [N II] λ6548+/Hβ ratio seems to correlate with the [N I]/Hβ ($R = 0.69$, Figure 6(c)) while the [N II] λ5755/Hβ has no correlation with [N I]/Hβ ($R = -0.03$, Figure 6(d)). Note that [N II] λ6548+/λ5755 is sensitive to electron temperature (see Section 3.2). Then, the different trends seen in Figures 6(c) and (d) imply the variation of temperature inside the remnant. However, we should be cautious to interpret the trends because those with large [N I]/Hβ ratios (i.e., [N I]/H$\beta \gtrsim 0.7$) also have relatively large uncertainties, and those with the large [N I]/Hβ ratios (except one data point from F82) do not appear in Figure 6(d) due to nondetection of the [N II] λ5755 line. The presence of the

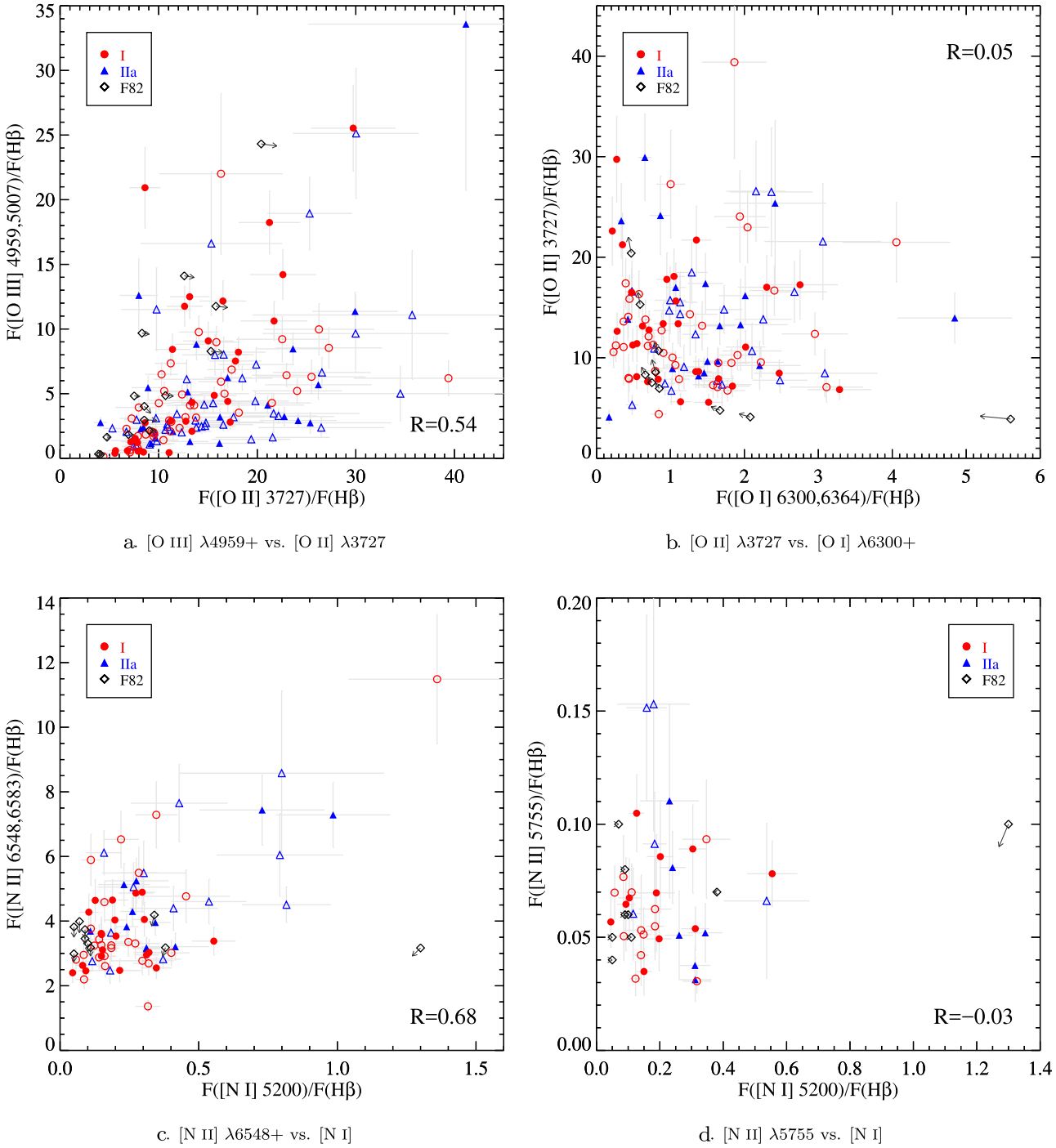

Figure 6. Correlation between line ratios of the same elements (oxygen and nitrogen) with different transitions. Panel (a): [O III] λ4959+ vs. [O II] λ3727; panel (b): [O II] λ3727 vs. [O I] λ6300+; panel (c): [N II] λ6548+ vs. [N I]; and panel (d): [N II] λ5755 vs. [N I]. All line intensities are normalized to Hβ.

correlation should be further examined with high signal-to-noise data.

3.2. Optical Properties: Electron Temperature and Density

Electron temperatures of ionized plasma are commonly derived from a set of forbidden line emission emitted by metastable levels of positive ions, such as [O III], [N II], and [S II]. A main representative is the ratio of [O III] $\lambda4959+/\lambda4363$ (e.g., Osterbrock & Ferland 2006, OF06, hereafter). The [O III] ratios in comparison with the [O III] $\lambda4959+$ intensities relative to Hβ are shown in Figure 7 (left panel). Adopting the exponential approximation of OF06 expressed as

$$\frac{j_{\lambda4959}+j_{\lambda5007}}{j_{\lambda4363}}=\frac{7.90\exp(3.29\times10^4/T)}{1+4.5\times10^{-4}n_e/T^{1/2}}, \quad (1)$$

[O III] line temperatures for Group I and IIa are estimated in Figure 7 (right panel). In addition, we calculate theoretical ratios at a density of 100 cm^{-3} using version 8 of the CHIANTI database (Dere et al. 1997; Del Zanna et al. 2015), which are overlaid with a dotted line. CHIANTI consists of critically evaluated set of up-to-date atomic data, together with user-friendly programs written

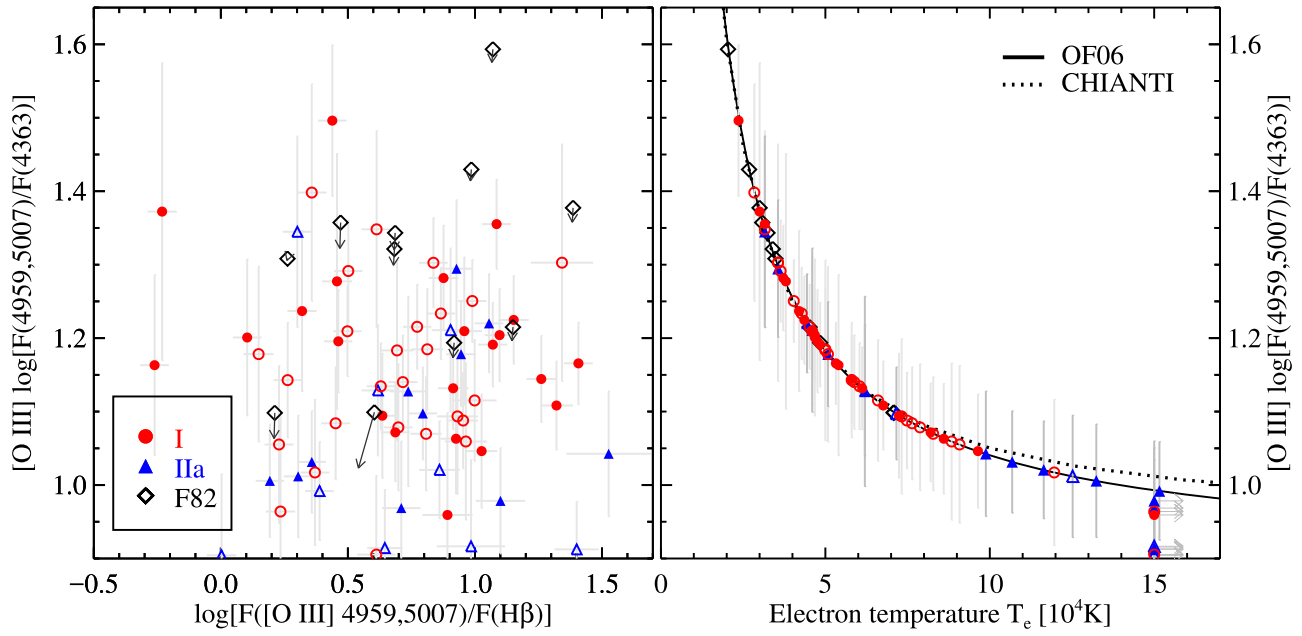

Figure 7. Left panel: comparison between [O III] line temperatures and [O III] λ4959+ line intensities relative to Hβ for Group I and IIa spectra (circles and triangles, respectively). Data from F82 are also overlaid (diamonds). Right panel: electron temperatures derived from the [O III] ratios using the exponential approximation of OF06 (solid line). The CHIANTI model calculation is also overlaid (dotted line) for comparison. See Section 3.2 for details.

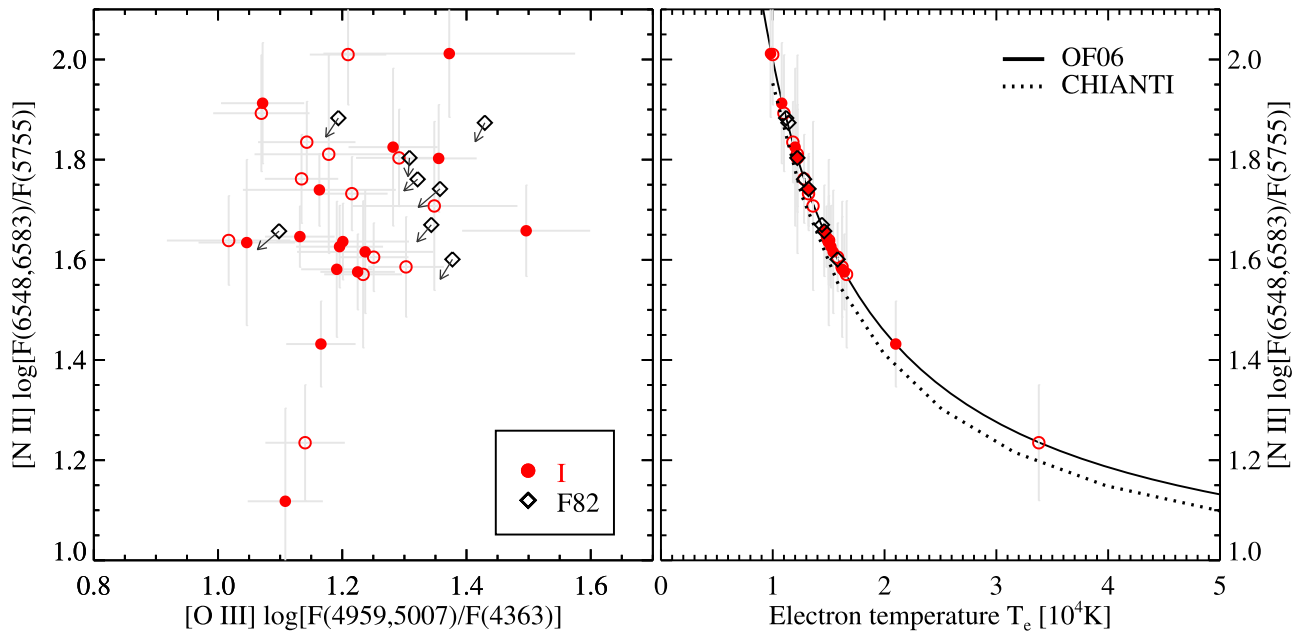

Figure 8. Left panel: comparison between [N II] and [O III] diagnostic of electron temperature. As the [N II] λ5755 line is mostly weak and contaminated in Group IIb spectra, only Group I is used here. Line ratios from F82 are also overlaid (diamonds). Right panel: electron temperatures derived from the [N II] ratios using CHIANTI (dotted line). See Section 3.2 for details.

in Interactive Data Language and Python to calculate the spectra from optically thin, collision-dominated astrophysical plasma.[10] Up to ~50,000 K, the ratios from CHIANTI are consistent with those from the exponential approximation, but they start to deviate at higher temperatures.

Overall, [O III] temperatures from Group I and IIa spectra range between ~30,000 K and 80,000 K, which are in good agreement with previous estimates (e.g., Miller 1974; Fesen et al. 1982). However, a few cases with the [O III] ratios less than ~10 indicate that the temperature exceeds ~10^5 K, which is above the equilibrium formation temperature. Such a high temperature has been reported previously (e.g., $T_e \gtrsim$ 80,000 K, Sankrit et al. 2014), which would occur in the narrow ionization zone just behind an X-ray producing (nonradiative) shock (e.g., Blair et al. 2005). The emission from these regions, however, could be too faint to be detected by LAMOST. Hence, there is a possibility that the overestimation of the [O III] λ4363 intensity leads the [O III] ratios to be less than ~10. Fitting its underlying baseline is sometimes uncertain due

[10] http://www.chiantidatabase.org

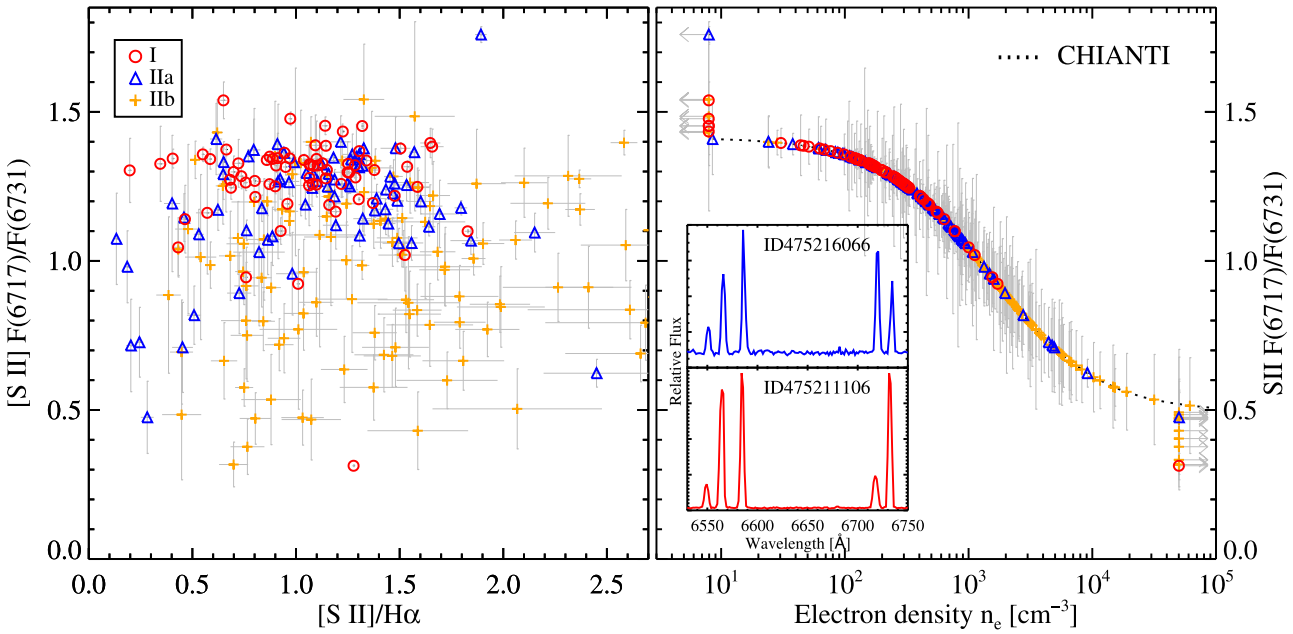

Figure 9. Left panel: [S II] line ratio diagnostic of electron density in comparison with [S II] λ6717+/Hα. Group I, IIa, and IIb spectra are denoted with circles, triangles, and crosses, respectively. Right panel: [S II] electron density estimates by using CHIANTI. Two insets present the zoomed-in spectra showing two extreme cases (obs. ID 475211106 and 475216066) showing [S II] ratios of ~0.31 and 1.76, respectively.

to the presence of absorption features nearby. In fact, Group IIa spectra, which are more affected by stellar features, tend to have lower [O III] ratios than Group I spectra, implying that the overestimation of [O III] λ4363 is conceivable.

Another temperature diagnostic is the ratio of [N II] λ6548+/λ5755. In Figure 8, we compare the [N II] and the [O III] ratios and derive the [N II] temperature in the same manner as Figure 7. Again, adopting the exponential approximation of OF06, the theoretical [N II] ratio as a function of temperature (T) is given by

$$\frac{j_{\lambda6548}+j_{\lambda6583}}{j_{\lambda5755}}=\frac{8.23\exp(2.50\times10^4/T)}{1+4.4\times10^{-3}n_e/T^{1/2}}, \quad (2)$$

shown with a solid line in Figure 8 (right panel). Also, theoretical ratios from the CHIANTI database are overlaid with a dotted line. Note that the [N II] λ5755 line is poorly detected in most Group IIa spectra due to its faintness; hence, only Group I spectra are used to estimate [N II] temperature. The resultant [N II] temperatures are mostly between 10,000 and 15,000 K, which is substantially lower than those from the [O III] ratios (see Figure 7). Also, there is no clear correlation between [N II] temperatures and [O III] temperatures. The higher temperature inferred from [O III] with a higher ionization state and no correlation between [N II] and [O III] is a natural feature of a region behind a radiating shock, where cooling and recombination to the lower-ionization state occur in succession. This trend has been reported in the literature (e.g., Miller 1974; Fesen et al. 1982) and is also found in other SNRs. For example, Pauletti & Copetti (2016) show the spatial variations in temperature maps of the SNR N49 in the Large Magellanic Cloud, which clearly demonstrate higher temperatures for [O III] line ratios compared to the [S II], [O II], and [N II] temperatures and different spatial distribution of the temperatures through the SNR.

The line ratios of [S II] λ6717/λ6731 (e.g., Osterbrock & Ferland 2006) and [O II] λ3729/λ3726 (e.g., Pradhan et al. 2006) are among common diagnostic tools for deriving the electron density (n_e). As the latter pair is closely located in wavelength, it is not resolved in the LAMOST spectra ($R\sim1800$). In Figure 9 (left panel), we compare the [S II] λ6717/λ6731 ratios with the relative intensity of [S II] λ6717+. Because the [S II] doublet is clearly detected even in the Group IIb spectra in most cases, Group I, IIa, and IIb are used for the n_e estimate. The [S II] ratios mostly range between 1.0 and 1.5 while some outliers having extremely low or high values are present (see below).

Using the CHIANTI calculations, we estimate the electron density from the [S II] λ6717/λ6731 line ratios (Figure 9, right). [S II] electron densities mostly range between $\lesssim$20 and $\approx$500 cm^{-3}, which are consistent with previous estimates (e.g., Miller 1974; Fesen et al. 1982). Two significant outliers are the lowest (~0.31) and highest (~1.76) [S II] ratios, which come from obs. ID 475211106 (Group I) and 475216066 (Group IIa) spectra as shown in the insets. The two spectra clearly show different trends: [S II] λ6731 is much stronger than [S II] λ6717 in obs. ID 475211106, and vice versa for obs. ID 475216066. The ratios outside the range given by the high- ($\gtrsim$1.4) and low- ($\lesssim$0.5) density limits indicate measurement errors, which possibly result from the sky spectrum contaminated by the diffuse SNR emission or unapparent confusion with other emission sources (see more in Section 4.2).

4. Global Spectrum of the Cygnus Loop

Using the Group I spectra, we have constructed a single integrated spectrum, which can represent a global spectrum of the Cygnus Loop. Because all of the LAMOST spectra are only relatively flux calibrated (Section 2.1), absolute flux calibration is required to combine them. Generally, the absolute flux calibration needs spectra of standard stars under the same observing conditions. However, in the case of large spectroscopic surveys such as LAMOST, it is not straightforward to apply this strategy because it is impossible to obtain a sufficient number of spectra for standard stars every observing run. Thus,

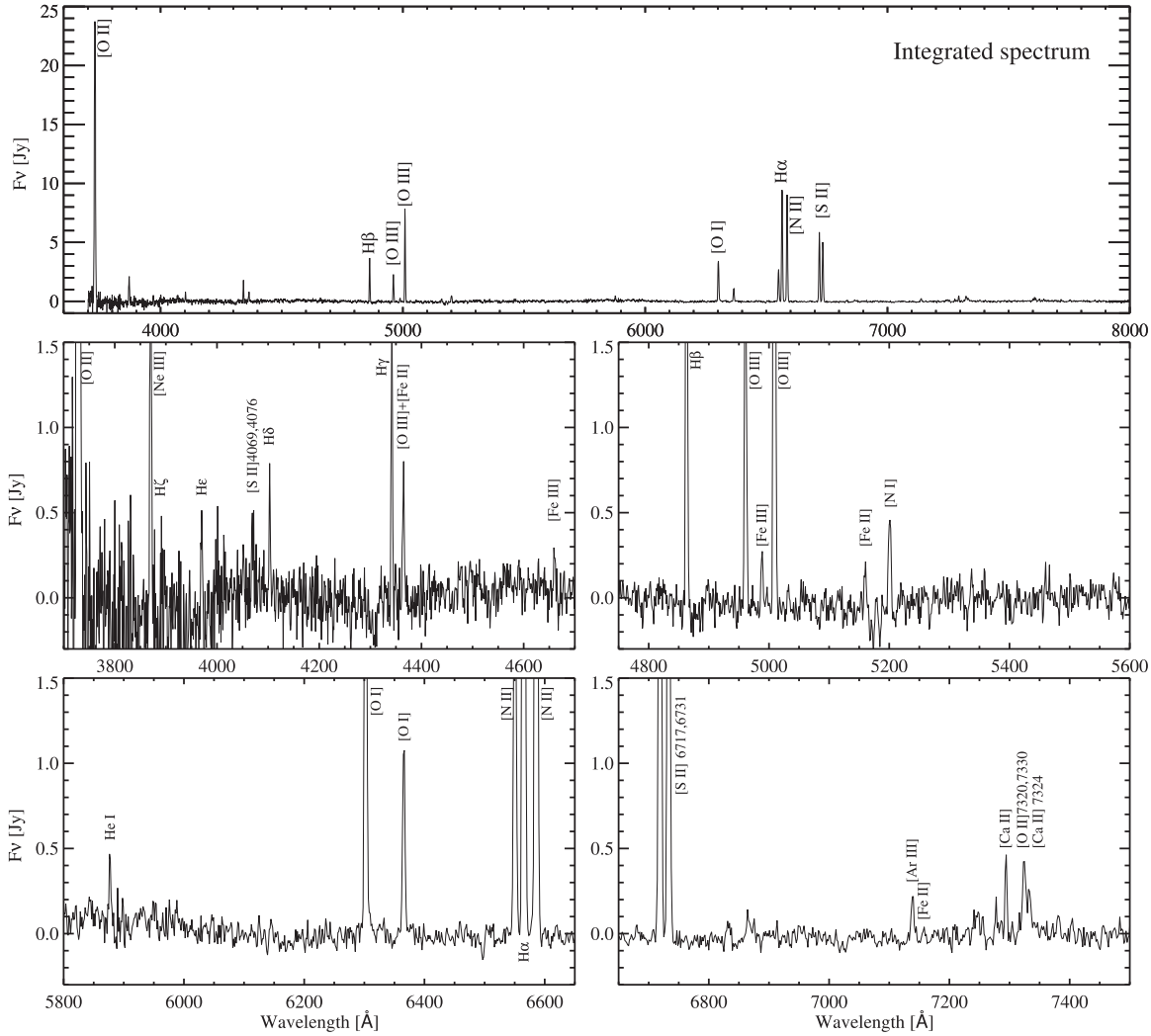

Figure 10. Global spectrum of the Cygnus Loop made of 75 Group I spectra (see Section 4 for details). An entire spectrum (3600–8000 Å) is shown in the top panel, while the other panels zoom in on segments of the same spectrum to discern weaker lines. Noticeable lines are marked.

Table 5
Line Intensities of the Global Emission Spectrum of the Cygnus Loop
($H\beta = 100$)

Ion ID	Wavelength (Å)	Intensity (Relative to $H\beta$)
[O II]	3727	1037
[Ne III]	3869	70
[O III]	4363	21
$H\beta$[a]	4864	100
[O III]	4959, 5007	298
[N I]	5200	20
[N II]	5755	6
[O I]	6300, 6364	175
[N II]	6548, 6584	443
$H\alpha$	6564	379
[S II]	6717	223
[S II]	6730	192

Note.
[a] Measured $H\beta$ flux is 1.34969 in counts.

instead of precise absolute flux calibration, we have carried out crude flux calibration based on photometric magnitudes (g and i bands), which are already used for co-adding spectra with multi-exposures during the LAMOST pipeline (Du et al. 2016). Following Equations (4)–(6) in Du et al. (2016), we have derived synthetic magnitudes and scale coefficients for each spectrum taking the Pan-STARRS1 g- and i-band transmission curves into account (Tonry et al. 2012). Then, the spectra are scaled using an average of the two scale coefficients and are accumulated into a single spectrum. After subtracting a continuum with a sixth-order polynomial fit, the final spectrum is obtained.

Figure 10 shows the global spectrum of the Cygnus Loop made by summing the 75 Group I spectra. The strongest emission in the spectrum is [O II] λ3727, and several forbidden lines as well as the Balmer series clearly appear. Close-up views of the spectrum show the presence of weak lines (e.g., [Fe II], [Fe III], [Ar III], [Ca II], and He I) too. In addition to the emission lines, contamination from stellar features (e.g., Mg I triplet at 5167, 5172, and 5183 Å) and residuals from imperfect sky subtraction (e.g., 6860–6960 Å due to telluric O_2) are also noticed. Intensities for detected emission lines are measured in the same way as described in Section 2.2, which are summarized in Table 5. One of the main results seen in Table 5 is the moderate [O III] λ4959+/$H\beta$ ratio of 2.98. Although the signature of incomplete shock (i.e., [O III] λ4959+/$H\beta \gtrsim 6$)

Table 6
Input Parameter of Ionization Levels in Shock Models

Parameter	Shock Model									
	F60	F80	F100	F120	F160	F200	P90	P100	P110	P130
v_s (km s^{-1})	60	80	100	120	160	200	90	100	110	130
pre-shock H I	0.0	0.0	0.0	0.0	0.0	0.0	0.62	0.32	0.0	0.0
pre-shock He I	0.84	0.28	0.07	0.03	0.02	0.0	0.95	0.66	0.0	0.0
pre-shock He II	0.16	0.72	0.92	0.95	0.85	0.58	0.05	0.34	0.93	0.80

Note. H is fully ionized and He is in ionization equilibrium in Model F, whereas H is partially ionized in Model P. The ionization fractions of H and He in model P are from Shull & McKee (1979).

has been reported from a considerable number of positions in the remnant (e.g., Fesen et al. 1982; Raymond et al. 1988), our result indicates that a fully radiative shock is the most representative shock characteristic of the Cygnus Loop. This is not surprising because the global spectrum is inevitably predominated by bright emission regions, which usually arise from radiative shocks (e.g., Raymond et al. 1988).

4.1. Shock Parameters

We investigate shock parameters to explain the measured line ratios of the global spectrum by using the shock code developed by Raymond (1979) and Cox & Raymond (1985) with updated atomic parameters. Among the parameters necessary for the calculation of the forbidden lines of O and S, we updated the electron collision strengths to the recently calculated ones for O I (Zatsarinny & Tayal 2003), O II (Kisielius et al. 2009), O III (Storey et al. 2014), and S II (Tayal & Zatsarinny 2010). The code assumes an 1D steady flow, using the Rankine–Hugoniot jump conditions to find the post-shock gas parameters. Then it uses the fluid equations to compute the density, temperature, and velocity as the gas cools. The perpendicular component of the magnetic field is assumed to be frozen in, and it is compressed with the gas as it cools. Time-dependent ionization calculations including photoionization are used to compute the cooling rate and the emissivities of spectral lines.

Shock emission analysis of individual filaments in the Cygnus Loop has been carried out in several previous studies (Miller 1974; Raymond 1979; Fesen et al. 1982; Hester et al. 1983; Raymond et al. 1988; Blair et al. 1991; Danforth et al. 2001, and references therein). According to these studies, the optical spectra of bright filaments can be modeled by either complete or incomplete shocks with shock speeds in the range of 60–140 km s^{-1} and ambient densities 4–20 cm^{-3}. We have run shock models for shock speed v_s = 60–200 km s^{-1} and pre-shock density n_0 = 10 cm^{-3}. For the magnetic field strength B_0, we adopt 5 μG, which is close to the median total magnetic field strength (6 μG) of the diffuse ($n \leqslant 300$ cm^{-3}) interstellar cloud (Heiles & Troland 2005; Crutcher et al. 2010). For the abundances of chemical elements, we use the solar abundances suggested by Asplund et al. (2009), Scott et al. (2015b), and Scott et al. (2015a). The abundances of the elements that show strong lines in the global spectrum are [N/H] = 7.83, [O/H] = 8.69, [Ne/H] = 7.93, and [S/H] = 7.12 where [X/H] is the log of number of X atoms per 10^{12} H atoms. One complication in shock modeling is the pre-shock ionization levels of H and He that affect the post-shock structure and, therefore, the emission-line fluxes (Raymond 1979; Shull & McKee 1979; Cox & Raymond 1985; Sutherland & Dopita 2017). We present a grid of models (Model F) where H is fully ionized and He is in ionization equilibrium with shock radiation. The presence of neutral H would have an effect similar to that of lowering the shock velocity at full ionization (Cox & Raymond 1985). For comparison, we also present a grid of models (Model P) where H is partially ionized. In this model, the ionization fractions of H and He are determined by balancing the upstream ionizing flux with the incoming ion flux, which is a good approximation for slow shocks (Shull & McKee 1979; Sutherland & Dopita 2017). At $v_s \geqslant 110$ km s^{-1}, H is fully ionized in model P, and the difference between the two models becomes negligible. Hence, we present Model F with v_s = 60–200 km s^{-1}, whereas Model P with v_s = 90–130 km s^{-1} are used for comparison. Pre-shock ionization levels of the these cases are summarized in Table 6. Finally, the models do not include emission from the photoionization precursor, which can be important for shocks faster than about 150 km s^{-1} (Dopita & Sutherland 1996). However, the precursor emission is faint and diffuse, so its contribution in a 2.″2 fiber would be small.

The measured line ratios are compared with the model calculations in Table 7. Considering that bright filaments in the Cygnus Loop are often assumed to have typical shock velocities around 100 km s^{-1} in the literature, most models in Table 7 (i.e., $v_s \gtrsim 80$ km s^{-1}) can reasonably reproduce the measurements within a factor of two or three. Models F120 and P110 show good agreement in the temperature-sensitive ratios (especially for [N II] λ6548+/5755 ratios), consequently tracing shock velocity but predicting slightly large [O III] λ4959+/Hβ and small [O II] λ3727+/[O III] λ4959+ ratios. In fact, all models except F60 and P90 produce lower [O II]/[O III] ratios than the observed one, and all but F60, P90, and F200 give higher [O III]/Hβ than the observed. This may indicate a mixture of low- ($\lesssim$100 km s^{-1}) and high-speed shocks with the presence of partially ionized H. In addition, the observed [O II] λ3727+/[O III] λ4959+ ratio higher, which is than those shown in most of the shock models, could result from depletion of carbon and silicon since [O II] λ3727 +/[O III] λ4959+ is sensitive to these elemental abundances (Raymond 1979; Fesen et al. 1982).

Note that the F120 or P110 models are not necessarily the best shock models to explain the global spectrum. Because we do not compare all measurable line ratios between the data and the models, it could be unfair to choose the best shock model to describe the global properties of the Cygnus Loop just based on Table 7. However, the current results verify that the global spectrum can be characterized by fast ($v_s \gtrsim 100$ km s^{-1}), radiative shocks and suggest the necessity of modifying the model parameters such as the elemental abundances. We will make detailed comparisons among different shock models and also discuss the spatial variation of shock parameters in our forthcoming paper.

Table 7
Line Ratios of the Global Spectrum with Shock Models

Ratio	Observed Value	Shock Model									
		F60	F80	F100	F120	F160	F200	P90	P100	P110	P130
[O III]4959+/Hβ	2.98 ± 0.39	0.13	5.19	5.09	4.91	3.86	2.93	0.28	3.78	4.96	5.24
[O II]3727+/[O III]4959+	3.47 ± 0.45	88.03	1.45	1.27	1.29	1.36	2.08	20.74	1.30	1.28	1.15
[O III]4959+/4363	14.1 ± 2.3	17.94	17.59	17.80	17.99	15.89	16.65	17.32	17.42	18.04	16.74
[N II]6548+/5755	71.4 ± 6.0	34.18	40.83	59.62	77.71	100.88	110.11	35.43	48.55	69.23	79.39
[N II]6548+/[O II]3727	0.43 ± 0.06	0.16	0.20	0.29	0.38	0.44	0.48	0.16	0.24	0.34	0.39
Hα/[N II]6548+	0.86 ± 0.12	1.81	2.20	1.62	1.23	1.29	0.99	3.21	2.54	1.41	1.27
Hα/[S II]6717+	0.92 ± 0.12	2.13	2.08	1.13	0.84	1.05	0.84	3.75	2.05	0.95	0.91
[S II] 6717/6731	1.16 ± 0.18	1.31	1.25	1.24	1.22	1.09	1.07	1.23	1.22	1.24	1.19

4.2. Discussion

One of the main results that the LAMOST data show is that the line intensities inside the remnant vary more significantly than was previously thought, perhaps because earlier studies selected bright filaments. The uncertainties in the LAMOST data that cannot be explicitly estimated would account for some of the variation (see below). However, the large variation in the line ratios can still have an important impact on understanding the evolutionary stages of SNRs as well as characteristics of extragalactic SNRs, particularly because a small variation in line strength within a single SNR is often a fundamental assumption for these studies (e.g., Daltabuit et al. 1976; Fesen et al. 1985). The most commonly used ratios for that purpose are Hα/[N II] λ6548+, Hα/[S II] λ6717+, and [S II] λ6717/λ6731 (e.g., Blair & Kirshner 1985; Fesen et al. 1985; Lee et al. 2015; Winkler et al. 2017). The former two ratios probe the N/H and (to some degree) S/H abundances, consequently representing local metallicity, and the [S II] doublet ratio is a well-known diagnostic of electron density. As the total number of spectroscopic pointings inside the Cygnus Loop increases more than an order of magnitude compared to previous studies, it would be meaningful to provide new ranges of these line ratios and to revisit their trends.

Figure 11 shows histogram distributions of Hα/[N II] λ6548 +, Hα/[S II] λ6717+, and [S II] λ6717/λ6731. Group I and IIa spectra are included for all cases, and Group IIb are also used for the [S II] doublet the same as Figure 9 shows. The distributions of Group I spectra (red bars in Figure 11) show that the ranges of the Hα/[N II] λ6548+, Hα/[S II] λ6717+, and [S II] λ6717/λ6731 ratios are 0.42–2.84, 0.55–5.07, and 0.31–1.54, respectively. When Group IIa are included, these ranges increase by a factor of 2–3 whereas the case of the [S II] doublet does not show much change even if Group IIb are included. This suggests that the presence of Group IIa outliers that significantly increase the ratio range are likely due to some errors resulting from imperfect subtraction of the Hα absorption feature. In addition, we also note that the ratio range of those with $2.9 \leqslant$ Hα/H$\beta \leqslant 4.0$ in Group I (i.e., excluding those with large uncertainties in the Balmer line ratio, Section 2.2) is as wide as that of all Group I. In fact, it is a natural consequence that uncertainties related to Hα/Hβ such as a mismatch between blue and red spectra or any calibration errors depending on wavelength cannot affect these ratios significantly as the Hα, [N II] λ6548+, and [S II] λ6717+ lines are located very closely to each other.

Fesen et al. (1985) collected previous observational results about these ratios in several Galactic SNRs (see their Table 5). The minimum and maximum values of each ratio combining all previous studies of the Cygnus Loop in their table are 0.66–1.25, 0.61–1.76, and 1.00–1.51 for Hα/[N II] λ6548+, Hα/[S II] λ6717+, and [S II] doublet, respectively (marked with dotted lines in Figure 11). Note that the largest number of observations included in Fesen et al. (1985) is 18 (Parker 1964) while the number of Group I and IIa spectra are 75 and 79, respectively. We examine the Group I spectra that give significantly large Hα/[N II] λ6548+ ($\gtrsim$1.5) and Hα/[S II] λ6717+ ($\gtrsim$2.0) ratios. There are six and five Group I spectra with such large Hα/[N II] λ6548+ and Hα/[S II] λ6717+, respectively, and four of them are in common. All of these outliers except one (obs. ID 470503149) show strong [O III] λ4959+ emission relative to Hβ, and more than half have [O III] λ4959+/H$\beta \gtrsim 6$ implying their association with incomplete shocks. It is clear that the line ratios resulting from the LAMOST data are more diverse than those in the literature although a part of this diversity is due to the errors in the LAMOST ratios. For [S II] λ6717/λ6731, most of Group I (and IIa) spectra well agree with the previous range except the one (obs. ID 475211106) as noted in Figure 9. This is reasonable because its variation is tightly constrained by electron density. As mentioned in Section 3.2, however, the spectrum of obs. ID 475211106 is problematic since its [S II] doublet ratio is smaller than the high-density limit (i.e., lower than 0.5). It is difficult to explain such a low ratio by any common errors including calibration, data reduction, and background confusion, because the emission lines including [S II] doublet in that spectrum are clearly detected with high S/Ns and their line profiles are also well-shaped (i.e., no possible residuals from sky subtraction). Further observations with high spatial precision and high spectral resolution are needed to clarify the origin of this abnormal ratio.

The mean values μ (standard deviation) of the ratios are 1.04 (0.45), 1.13 (0.64), and 1.27 (0.16) for Hα/[N II] λ6548+, Hα/[S II] λ6717+, and [S II] doublet, respectively, when Group I spectra are only considered. These values are changed when Group IIa (and IIb) spectra are included, but the change is not significant. Corresponding mean values listed in Fesen et al. (1985) range from 0.88–0.99, 1.00–1.08, and 1.19–1.40, respectively, which well agree with the newly measured μ despite the diversity of the ratio ranges that Group I (and IIa) show. In other words, although the standard deviations of the line ratios are larger than the previous measurements, their mean values are overall consistent. This result implies that as the number of observations (i.e., area that spectroscopy covers) increases, the range of the line ratios might widen, but their mean values can remain the same. This supports the validity of

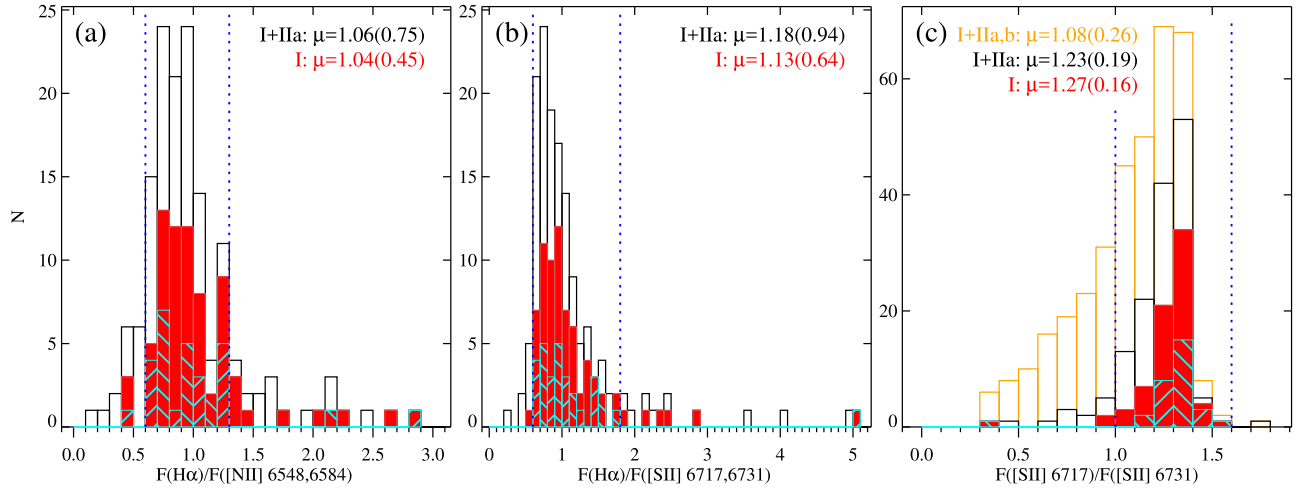

Figure 11. Line-intensity variations inside the Cygnus Loop: (a) Hα/[N II] λ6548+, (b) Hα/[S II] λ6717+, and (c) [S II] λ6717/λ6731. Ratio distributions of Group I and IIa (black lines) and Group I only (red bars) are presented in all panels, and Group IIb (yellow lines) are also included in panel (c). Those in Group IIa having extremely large ratios are not shown but are included in all analysis. A subset of Group I that has $2.9 \leqslant$ Hα/H$\beta \leqslant 4.0$ is differentially marked (cyan shade). Two dotted lines indicate the minimum and maximum ratios that have been reported in the literature (see the text). The mean (μ) of each ratio with standard deviation (in parenthesis) is noted in each panel.

these line ratios as a probe of the evolutionary state or as a tracer of the elemental abundance of the ambient medium.

Another aspect that the LAMOST data, particularly those from the faint filaments, show is the possible contribution of background emission including the precursor emission, the Galactic Hα emission, and the Geocoronal Hα. By targeting bright filaments in the Cygnus Loop, previous studies (e.g., Fesen et al. 1982, 1985, and references therein) can consequently minimize (and subtract off) the background contribution in their sample spectra. The slightly lower Hα/[N II] λ6548+ and Hα/[S II] λ6717+ ratios reported in Fesen et al. (1985) than those derived from the LAMOST data could be explained by this. On the contrary, the spectra of poorly resolved (e.g., the Magellanic Clouds) or unresolved (other distant galaxies) SNRs can be affected by these background sources more significantly. In particular, the precursor emission is very diffuse, so its contribution to a global spectrum of an extragalactic SNR would not be negligible compared to bright filaments of the Cygnus Loop or any other bright filaments of Galactic SNRs studied earlier. We will examine the effect of the precursor using shock models in the forthcoming paper.

It is worthwhile to point out that the corresponding ratios of the global spectrum, referred to as "global ratios" hereafter (0.86, 0.92, and 1.16, see Table 7), are systematically lower than the μ values. In particular, since a single spectrum obtained from a spatially unresolved SNR in an external galaxy would be analogous to the global spectrum, it is critical to understand features of the global spectrum and how to interpret them correctly. The global spectrum can be considered to be the brightness-weighted summation while μ is a result of unweighted summation. When outliers have extremely large or small ratios, this can affect μ regardless of their brightness but less so for the global spectrum if the outliers are rather faint. On the other hand, the global spectrum is always dominated by spectra with high surface brightness. In the case of Group I (and IIa), there are particularly large Hα/[N II] λ6548+ and Hα/[S II] λ6717+ ratios so that the μ values become relatively larger than those of the global spectrum. Interestingly, the [S II] doublet ratio of the global spectrum is smaller than μ of Group I, indicating that the bright Group I spectra tend to have small [S II] ratios tracing high-density regions. This is consistent with the aforementioned description of the global spectrum, which represents the bright spectra usually emitted by dense material swept-up by radiative shocks.

To avoid the effect of the outliers, a median value of each ratio is also examined: 0.92. 0.94, and 1.31 for Hα/[N II] λ6548+, Hα/[S II] λ6717+, and [S II] doublet, respectively, in the case of Group I spectra. The smaller values for Hα/[N II] λ6548+ and Hα/[S II] λ6717+ and larger one for the [S II] doublet compared to μ are a natural consequence of the outliers. These median values can be interpreted as the most common ratios from the sample spectra. Comparing the median ratios with the global ratios, the Hα/[N II] λ6548+ and Hα/[S II] λ6717+ ratios show better consistency than μ, but the global [S II] ratio is again smaller than the median. The better agreement seen in the former two line ratios could support their validity, meaning that these ratios from the global spectrum can probe the overall abundance of the SNR. This can be reasonable if emitting material inside an SNR is mostly ambient ISM with uniform abundance. However, in the case of young core-collapse SNRs where newly formed ejecta can significantly contribute, a global spectrum might give a misleading value for the abundances of the SNR. In the case of [S II] doublet, it again shows that the ratio of the global spectrum is smaller than the median value. Hence, this further suggests that the electron density measured from the global spectrum is likely to be biased toward denser regions.

5. Summary

We have examined the prototypical middle-aged SNR, the Cygnus Loop, using unbiased spectroscopic data obtained with LAMOST. Both its large field of view ($\sim$20 deg^2), nearly as large as the size of the Loop, and the multi-object spectrographs that can obtain 4000 spectra simultaneously provide a unique opportunity to spectroscopically study the entire SNR en masse. In the field of the Cygnus Loop, 2747 spectra are found in the LAMOST DR5, and 368 spectra are confirmed to exhibit emission lines originating from the SNR. In this paper,

we describe the basic information on the LAMOST data and the classification of the spectra, and examine the correlation of the line ratios and the global spectrum of the SNR. The primary results are as follows.

1. Based on the presence of emission lines associated with the SNR and the contamination from background/foreground stars, 75, 79, and 214 spectra are classified into Groups I, IIa, and IIb, which represent SNR-dominated emission, clear SNR emission with stellar features, and relatively weak SNR emission with dominant stellar features, respectively. Besides, 176 spectra exhibit emission lines, the origins of which are inconclusive (categorized into Group III). As the spatial distribution of this Group is mostly near the bright filaments, it is likely that the Group III spectra are also associated with the Cygnus Loop.
2. Combining the 75 Group I and 79 Group IIa spectra, the 154 spectra are further examined in detail. Various emission lines are identified, and relative intensities of the key lines are measured. The relative strengths of line emission show the spatial variation; In particular, wide ranges of [O III] $\lambda4959+/\mathrm{H}\beta$ and other line ratios such as [O II] $\lambda3727/\mathrm{H}\beta$, [N II] $\lambda6548+/\mathrm{H}\beta$ indicate the diversity of the physical parameters coexisting inside the single SNR.
3. Line ratios of different elements with the same ionization state generally show systematic correlations. The [S II] $\lambda6717+/\mathrm{H}\alpha$ ratio, a well-known shock diagnostic, appears to correlate well with [N II] $\lambda6548+/\mathrm{H}\alpha$, whereas [O I] $\lambda6300+/\mathrm{H}\alpha$ shows no clear evidence of correlation. This implies that [N II] $\lambda6548+/\mathrm{H}\alpha$ is more reliable secondary shock tracer than [O I] $\lambda6300+/\mathrm{H}\alpha$.
4. Electron temperatures estimated with the [O III] ratio mostly range between $\sim$3–8 $\times$ 10^4 K while those with the [N II] ratio range between $\sim$1–1.5 $\times$ 10^4 K. The difference between the two estimates is a natural feature for a region behind a radiative shock, where cooling and recombination to the lower-ionization state occur in succession. The electron density of the Cygnus Loop is mostly between 20 and 500 cm^{-3} while some outliers indicate observational uncertainties.
5. The global spectrum of the Cygnus Loop demonstrates characteristics of a fully radiative shock albeit the presence of incomplete shocks inside the remnant. Comparison between the line ratios of the global spectrum and shock models verifies that fast (v_s = 100–140 $\mathrm{km\,s}^{-1}$), radiative shocks can explain the observed ratios reasonably well but also suggests local variations of the shock parameters as well as the possible depletion of carbon and silicon.
6. Group I and IIa spectra show wider ranges of the line ratios ($\mathrm{H}\alpha/$[N II] $\lambda6548+$, $\mathrm{H}\alpha/$[S II] $\lambda6717+$, and [S II] $\lambda6717/\lambda6731$) than those previously reported. This implies that local variations in physical properties inside a single SNR can be more significant than commonly assumed, though uncertainties in the fluxes also contribute. In addition, the median values of the former two ratios are consistent with the corresponding ratios derived from the global spectrum while the median of the [S II] doublet is larger than that from the global ratio. These results suggest that an optical spectrum of an unresolved, extragalactic SNR can probe its overall elemental abundance reasonably well, while its density diagnostics tend to overestimate its density.

In our forthcoming papers, we will make detailed comparisons among different shock models, examine the spatial variation of shock properties inside the Cygnus Loop, and perform an analysis of kinematics. A combination of a low/medium-resolution multi-object spectrograph with a large field of view and multiwavelength imaging surveys including the SNR and its neighboring regions will complete our understanding of the Cygnus Loop on a large scale and will benefit the interpretation of distant SNRs.

J.Y.S. and G.Z. were supported by NSFC grant Nos. 11988101, 11650110436, and 11890694, and J.Y.S. thanks the Chinese Academy of Sciences (CAS) for support through LAMOST fellowship. B.-C.K. acknowledges support from the Basic Science Research Program through the National Research Foundation of Korea (NRF) funded by the Ministry of Science, ICT and future Planning (2017R1A2A2A05001337). Funding for LAMOST (http://www.lamost.org) has been provided by the National Development and Reform Commission. LAMOST is operated and managed by the National Astronomical Observatories, Chinese Academy of Sciences. CHIANTI is a collaborative project involving George Mason University, the University of Michigan (USA), University of Cambridge (UK) and NASA Goddard Space Flight Center (USA).

Appendix
LAMOST Spectra of the Group I Sample at the Entire Wavelengths

The 75 Group I spectra are displayed in Figure A1 with their Obs. IDs. Prominent emission lines clearly appear (marked with blue dashed lines). Well-known stellar absorption features (Ca, K, and H; G(Ca+Fe); Mg I b triplet; Na D1 and D2; Ca II triplet) are marked with orange dashed lines, which are mostly weak or inconspicuous.

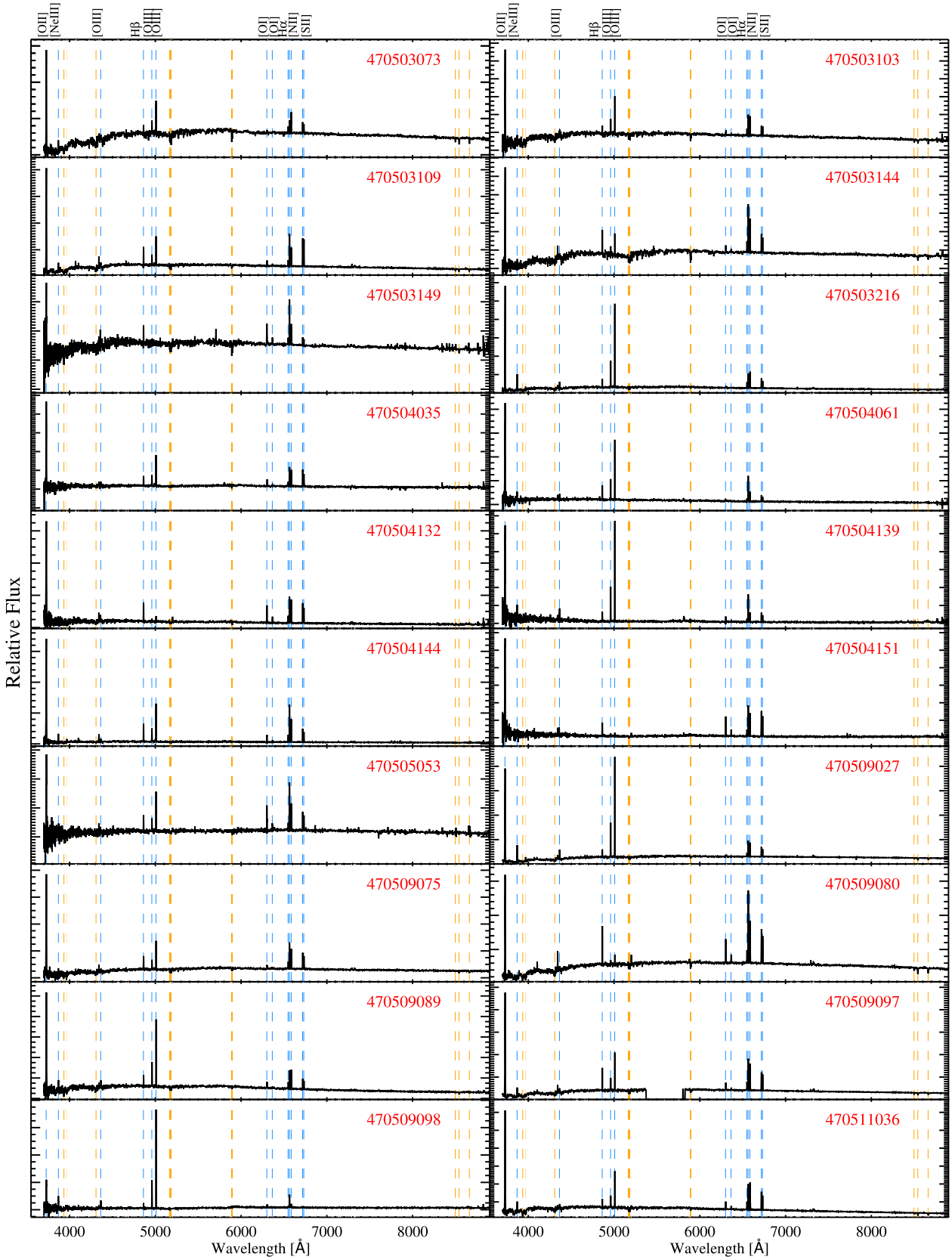

Figure A1. LAMOST data of 75 Group I spectra at the entire wavelengths (3500–8900 Å). Obs. ID is marked in each panel. Major emission lines are identified with labels at top (blue lines), and several stellar absorption features are also marked (orange lines). The complete figure set (4 images) is available in the online journal. (The complete figure set (4 images) is available.)

ORCID iDs

Ji Yeon Seok https://orcid.org/0000-0002-0070-3246
Gang Zhao https://orcid.org/0000-0002-8980-945X
John C. Raymond https://orcid.org/0000-0002-7868-1622

References

Arendt, R. G., Dwek, E., & Leisawitz, D. 1992, ApJ, 400, 562
Asplund, M., Grevesse, N., Sauval, A. J., et al. 2009, ARA&A, 47, 481
Bai, Z.-R., Zhang, H.-T., Yuan, H.-L., et al. 2017, RAA, 17, 091
Bilikova, J., Williams, R. N. M., Chu, Y.-H., Gruendl, R. A., & Lundgren, B. F. 2007, AJ, 134, 2308
Blair, W. P., & Kirshner, R. P. 1985, ApJ, 289, 582
Blair, W. P., Long, K. S., Vancura, O., et al. 1991, ApJL, 379, L33
Blair, W. P., Sankrit, R., & Raymond, J. C. 2005, AJ, 129, 2268
Braun, R., & Strom, R. G. 1986, A&A, 164, 208
Chevalier, R. A. 1974, ApJ, 188, 501
Chevalier, R. A., & Raymond, J. C. 1978, ApJL, 225, L27
Chu, Y.-H. 1997, AJ, 113, 1815
Cox, D. P., & Raymond, J. C. 1985, ApJ, 298, 651
Crutcher, R. M., Wandelt, B., Heiles, C., Falgarone, E., & Troland, T. H. 2010, ApJ, 725, 466
Cui, X.-Q., Zhao, Y.-H., Chu, Y.-Q., et al. 2012, RAA, 12, 1197
Daltabuit, E., Dodorico, S., & Sabbadin, F. 1976, A&A, 52, 93
Danforth, C. W., Blair, W. P., & Raymond, J. C. 2001, AJ, 122, 938
Danforth, C. W., Cornett, R. H., Levenson, N. A., Blair, W. P., & Stecher, T. P. 2000, AJ, 119, 2319
Del Zanna, G., Dere, K. P., Young, P. R., et al. 2015, A&A, 582, A56
Deng, L.-C., Newberg, H. J., Liu, C., et al. 2012, RAA, 12, 735
Dere, K. P., Landi, E., Mason, H. E., et al. 1997, A&AS, 125, 149
Dopita, M. A., & Sutherland, R. S. 1996, ApJS, 102, 161
Draine, B. T., & McKee, C. F. 1993, ARA&A, 31, 373
Du, B., Luo, A.-L., Kong, X., et al. 2016, ApJS, 227, 27
Fesen, R. A., Blair, W. P., & Kirshner, R. P. 1982, ApJ, 262, 171
Fesen, R. A., Blair, W. P., & Kirshner, R. P. 1985, ApJ, 292, 29
Fesen, R. A., & Hurford, A. P. 1996, ApJS, 106, 563
Fesen, R. A., Weil, K. E., Cisneros, I. A., Blair, W. P., & Raymond, J. C. 2018, MNRAS, 481, 1786
Ghavamian, P., Raymond, J., Smith, R. C., & Hartigan, P. 2001, ApJ, 547, 995
Ghavamian, P., Schwartz, S. J., Mitchell, J., et al. 2013, SSRv, 178, 633
Gordon, S. M., Kirshner, R. P., Long, K. S., et al. 1998, ApJS, 117, 89
Graham, J. R., Levenson, N. A., Hester, J. J., Raymond, J. C., & Petre, R. 1995, ApJ, 444, 787
Heiles, C., & Troland, T. H. 2005, ApJ, 624, 773
Hester, J. J., & Cox, D. P. 1986, ApJ, 300, 675
Hester, J. J., Parker, R. A. R., & Dufour, R. J. 1983, ApJ, 273, 219
Hester, J. J., Raymond, J. C., & Blair, W. P. 1994, ApJ, 420, 721
Hines, D. C., Rieke, G. H., Gordon, K. D., et al. 2004, ApJS, 154, 290
Hummer, D. G., & Storey, P. J. 1987, MNRAS, 224, 801
Hwang, U., Laming, J. M., Badenes, C., et al. 2004, ApJL, 615, L117
Katagiri, H., Tibaldo, L., Ballet, J., et al. 2011, ApJ, 741, 44
Katsuda, S., Maeda, K., Ohira, Y., et al. 2016, ApJL, 819, L32
Kim, I.-J., Seon, K.-I., Lim, Y.-M., et al. 2014, ApJ, 784, 12
Kisielius, R., Storey, P. J., Ferland, G. J., et al. 2009, MNRAS, 397, 903
Koo, B.-C., Lee, J.-J., Jeong, I.-G., Seok, J. Y., & Kim, H.-J. 2016, ApJ, 821, 20
Leahy, D. A. 2002, AJ, 123, 2689
Leahy, D. A., & Roger, R. S. 1998, ApJ, 505, 784
Leahy, D. A., Roger, R. S., & Ballantyne, D. 1997, AJ, 114, 2081
Lee, J.-J., Koo, B.-C., Snell, R. L., et al. 2012, ApJ, 749, 34
Lee, M. G., Sohn, J., Lee, J. H., et al. 2015, ApJ, 804, 63
Levenson, N. A., Graham, J. R., Aschenbach, B., et al. 1997, ApJ, 484, 304
Levenson, N. A., Graham, J. R., Hester, J. J., & Petre, R. 1996, ApJ, 468, 323
Levenson, N. A., Graham, J. R., Keller, L. D., & Richter, M. J. 1998, ApJS, 118, 541
Levenson, N. A., Graham, J. R., & Snowden, S. L. 1999, ApJ, 526, 874
Levenson, N. A., Kirshner, R. P., Blair, W. P., & Winkler, P. F. 1995, AJ, 110, 739
Long, K. S. 1985, SSRv, 40, 531
Long, K. S., Blair, W. P., Milisavljevic, D., Raymond, J. C., & Winkler, P. F. 2018, ApJ, 855, 140
Long, K. S., Blair, W. P., Vancura, O., et al. 1992, ApJ, 400, 214
Lopez, L. A., Ramirez-Ruiz, E., Huppenkothen, D., Badenes, C., & Pooley, D. A. 2011, ApJ, 732, 114
Luo, A.-L., Zhao, Y.-H., Zhao, G., et al. 2015, RAA, 15, 1095
Mathewson, D. S., & Clarke, J. N. 1973, ApJ, 180, 725
McKee, C. F., & Hollenbach, D. J. 1980, ARA&A, 18, 219
Medina, A. A., Raymond, J. C., Edgar, R. J., et al. 2014, ApJ, 791, 30
Miller, J. S. 1974, ApJ, 189, 239
Miyata, E., Tsunemi, H., Pisarski, R., & Kissel, S. E. 1994, PASJ, 46, L101
Osterbrock, D. E., & Ferland, G. J. 2006, in Astrophysics of Gaseous Nebulae and Active Galactic Nuclei, ed. D. E. Osterbrock & G. J. Ferland (2nd ed.; Sausalito, CA: Univ. Science Books), 2006
Parker, R. A. R. 1964, ApJ, 139, 493
Parker, R. A. R. 1967, ApJ, 149, 363
Patnaude, D. J., Fesen, R. A., Raymond, J. C., et al. 2002, AJ, 124, 2118
Pauletti, D., & Copetti, M. V. F. 2016, A&A, 595, A10
Peters, C. L., Lopez, L. A., Ramirez-Ruiz, E., Stassun, K. G., & Figueroa-Feliciano, E. 2013, ApJL, 771, L38
Pradhan, A. K., Montenegro, M., Nahar, S. N., & Eissner, W. 2006, MNRAS, 366, L6
Preite Martinez, A. 2011, A&A, 527, A55
Raymond, J. C. 1979, ApJS, 39, 1
Raymond, J. C. 1991, PASP, 103, 781
Raymond, J. C., Blair, W. P., Fesen, R. A., & Gull, T. R. 1983, ApJ, 275, 636
Raymond, J. C., Davis, M., Gull, T. R., & Parker, R. A. R. 1980, ApJL, 238, L21
Raymond, J. C., Hester, J. J., Cox, D., et al. 1988, ApJ, 324, 869
Reach, W. T., Rho, J., Jarrett, T. H., & Lagage, P.-O. 2002, ApJ, 564, 302
Rho, J., Jarrett, T. H., Cutri, R. M., & Reach, W. T. 2001, ApJ, 547, 885
Rho, J., & Petre, R. 1998, ApJL, 503, L167
Sankrit, R., Blair, W. P., Raymond, J. C., & Long, K. S. 2000, AJ, 120, 1925
Sankrit, R., Raymond, J. C., Bautista, M., et al. 2014, ApJ, 787, 3
Sankrit, R., Williams, B. J., Borkowski, K. J., et al. 2010, ApJ, 712, 1092
Scott, P., Asplund, M., Grevesse, N., et al. 2015a, A&A, 573, A26
Scott, P., Grevesse, N., Asplund, M., et al. 2015b, A&A, 573, A25
Seok, J. Y., Koo, B.-C., & Onaka, T. 2013, ApJ, 779, 134
Seon, K.-I., Han, W., Nam, U.-W., et al. 2006, ApJL, 644, L175
Shull, J. M., & McKee, C. F. 1979, ApJ, 227, 131
Smith, R. C., Kirshner, R. P., Blair, W. P., Long, K. S., & Winkler, P. F. 1993, ApJ, 407, 564
Storey, P. J., Sochi, T., & Badnell, N. R. 2014, MNRAS, 441, 3028
Stoughton, C., Lupton, R. H., Bernardi, M., et al. 2002, AJ, 123, 485
Sutherland, R. S., & Dopita, M. A. 2017, ApJS, 229, 34
Tayal, S. S., & Zatsarinny, O. 2010, ApJS, 188, 32
Tonry, J. L., Stubbs, C. W., Lykke, K. R., et al. 2012, ApJ, 750, 99
Uchida, H., Tsunemi, H., Katsuda, S., et al. 2009, ApJ, 705, 1152
Uyanıker, B., Reich, W., Yar, A., et al. 2002, A&A, 389, L61
Uyanıker, B., Reich, W., Yar, A., et al. 2004, A&A, 426, 909
Williams, R. M., Chu, Y.-H., Dickel, J. R., et al. 1999, ApJS, 123, 467
Winkler, P. F., Blair, W. P., & Long, K. S. 2017, ApJ, 839, 83
Xiang, M. S., Liu, X. W., Yuan, H. B., et al. 2015, MNRAS, 448, 90
Yamane, Y., Sano, H., van Loon, J. T., et al. 2018, ApJ, 863, 55
Zatsarinny, O., & Tayal, S. S. 2003, ApJS, 148, 575
Zhao, G., Zhao, Y.-H., Chu, Y.-Q., Jing, Y.-P., & Deng, L.-C. 2012, RAA, 12, 723